Title: The BR-body proteome contains a complex network of protein-protein and protein-RNA interactions

Authors: Nandana, V.[1]#, Rathnayaka-Mudiyanselage, I.W.[1,2]#, Muthunayake, N.S.[1*], Hatami, A.[3] Mousseau, C.B.[4], Ortiz-Rodríguez, L.A.[5], Vaishnav, J.[3$], Collins, M.[6], Gega, A.[1&], Mallikaarachchi, K.S.[1], Yassine, H.[1], Ghosh, A.[1], Biteen, J.S.[5], Zhu, Y.[3], Champion, M.M.[4], Childers, W.S.[6], Schrader, J.M.[1]
[1]Wayne State University, Department of Biological Sciences, Detroit, MI
[2]Wayne State University, Department of Chemistry, Detroit, MI
[3]Wayne State University, Department of Chemical Engineering and Materials Science, Detroit, MI
[4]University of Notre Dame, Department of Chemistry, Notre Dame, IN
[5]University of Michigan, Department of Chemistry, Ann Arbor, MI
[6]University of Pittsburgh, Department of Chemistry, Pittsburgh, PA
[#]These authors contributed equally
[&]Current affiliation: University of Toledo Medical School
[$]Current affiliation: University of Massachusetts-Amherst
*Current affiliation: Wayamba University of Sri Lanaka, Faculty of Medicine, Department of Biochemistry
Corresponding Author: Schrader@wayne.edu

Highlights

1. BR-body proteomics identified 111 proteins enriched in BR-bodies.
2. BR-bodies associate with an interconnected network of RNP condensates.
3. BR-body condensation is modulated by its interaction network.
4. RNA is required for rapid BR-body condensation.

Abstract

Bacterial RNP bodies (BR-bodies) are non membrane-bound structures that facilitate mRNA decay by concentrating mRNA substrates with RNase E and the associated RNA degradosome machinery. However, the full complement of proteins enriched in BR-bodies has not been defined. Here we define the protein substrates of BR-bodies through enrichment of the bodies followed by liquid chromatography-mass spec (LC-MS) proteomic analysis. We found 111 BR-body enriched proteins, including many RNA binding proteins, many of which are also recruited directly to *in vitro* reconstituted RNase E droplets, suggesting BR-bodies are more complex than previously assumed. While most BR-body enriched proteins cannot phase separate, we identified five which can undergo RNA dependent phase separation *in vitro*, suggesting other RNP condensates interface with BR-bodies. The RNA degradosome protein clients are recruited more strongly to RNase E droplets than that of the other RNP condensates, suggesting that client specificity is largely achieved through direct protein-protein interactions. We observe that some RNP condensates assemble unidirectionally, suggesting that RNA may be trafficked through RNP condensates in an ordered manner to facilitate mRNA processing/decay, and that some BR-body associated proteins have the capacity to dissolve the condensate. Finally, we find that RNA dramatically stimulates the rate of RNase E phase separation *in vitro*, explaining the observed dissolution of BR-bodies after cellular mRNA depletion observed previously. Altogether, these results suggest that a complex network of protein-protein and protein-RNA interactions controls BR-body phase separation while coordinating this mode of organization with RNA processing.

Introduction:

Biomolecular condensates have shown to be an important mode of subcellular organization in eukaryotes and bacteria[1–3]. As bacteria often lack membrane bound organelles, biomolecular condensates may provide a generalized strategy to their subcellular organization. Indeed, many bacterial biomolecular condensates have been recently identified in various species, including BR-bodies, signaling condensates, DNA replication condensates, RNApol condensates, Hfq condensates, Rubisco condensates, etc.[4–10]. Biomolecular condensates typically assemble through the physical process of phase-separation, which involves association of macromolecular scaffolds and segregation of other cellular components, ultimately leading to distinct non-membrane bounded structures[11]. Recent analyses of condensate physical properties appear to be consistent with a model of percolation-coupled phase separation, which includes both associative interactions as well as segregative[12] leading to phase separation[13]. Macromolecules which have the capacity to phase separate are referred to as scaffolds, which generally provide a platform for multi-valent interactions leading to phase separation and molecules that are recruited to condensates but cannot phase separate themselves are called clients[14] with the composition of scaffolds and clients that make up a condensate will determine the biochemical and cellular function. Importantly, molecules inside of condensates can often show diffusive dynamics, suggesting biomolecular condensates can facilitate biochemical processes within them[15,16]. Models have been suggested for how condensates might help accelerate enzyme catalyzed processes, including acceleration of reaction rates by local concentration, increased reaction specificity by selective recruitment of certain substrates and avoidance of others, and the ability to prevent release of pathway intermediates[17–19]. Conversely, they have been proposed to sequester substrate molecules from their enzymes leading to a reduction in reaction rates[20,21]. To determine the biochemical consequences of biomolecular condensate organization, an important goal is to be able to purify and reconstitute the essential molecular components of the condensate.

Despite advances in biomolecular condensate biochemistry, many *in vitro* studies have focused on purified scaffolds, and often lack the full suite of molecules identified to interact *in vivo*. This is potentially problematic, as proteomic/transcriptomic investigations of eukaryotic biomolecular condensates have revealed that biomolecular condensates are enriched in hundreds of different molecular species that may alter their biochemical or cellular functions. For example, P-bodies have been found to have >125 proteins and >6000 RNA transcripts[22], and importantly appear to help concentrate mRNA decay enzymes (including decapping enzymes, LSM proteins, Xrn1 nuclease, deadenylases, etc.) together with decapped translationally repressed mRNAs. Stress granules have been found to contain >300 proteins and >1800 RNA transcripts[23–25], often including a partially overlapping set of components with P-bodies[22,26], yet the differences in composition and slower dynamics[27] suggests that these structures likely have distinct functions. Through careful quantitative measurements, the core set of P-body proteins has recently been reconstituted *in vitro*, with similar dynamic propertiess[28]. In bacteria, BR-bodies were found to be enriched in long, poorly translated cellular mRNAs and sRNAs, a class of translational repressors, together with the RNA degradosome proteins[4,29]. Therefore, it was assumed that this structure might have a small set of protein clients that could be amendable to full *in vitro* reconstitution, however, the full complement of proteins in BR-bodies were not defined[27].

To define the proteome of *Caulobacter crescentus* BR-bodies, we performed a cellular enrichment by differential centrifugation[30] followed by quantitative liquid chromatography tandem mass

83 spectrometry (LC-MS). Similar to eukaryotic condensates, we identified over 100 proteins which were
84 enriched in BR-bodies. Enriched proteins tend to localize into foci *in vivo* and enter RNase E
85 condensates *in vitro*, suggesting many are likely direct clients of RNase E, the main scaffold of the BR-
86 body. While most enriched proteins do not assemble into biomolecular condensates *in vitro*, we
87 identified five BR-body associated proteins which can undergo phase-separation (phase separate
88 without RNase E), suggesting they form distinct RNP condensates in the cell that interact with RNase E.
89 By assaying the pairwise ability of each scaffold protein to mix with the others, we observed that some
90 pairs of scaffolds have strong associations, and that certain pairs show directional recruitment which
91 likely impacts RNP assembly order, leading to heterogenous RNP condensates *in vivo*. We also identified
92 two proteins which can dissolve BR-bodies both *in vivo* and *in vitro*, suggesting that they may negatively
93 regulate the cell's ability to assemble BR-bodies. Despite the identification of many BR-body associated
94 proteins, the RNA degradosome proteins are the only proteins identified that stoichiometrically bind to
95 RNase E[31], suggesting a minimal BR-body may be possible to reconstitute. Minimal BR-body phase
96 separation was kinetically stimulated by RNA, and showed similar RNase E FRAP dynamics to RNase E-
97 RNA droplets. Overall, this suggests that BR-bodies have similar complex interaction network to
98 eukaryotic RNP condensates, and the reconstitution of the "core" minimal BR-body components
99 provides an exciting framework to begin assessing their biochemical functions and how they might be
100 altered by the addition of BR-body associated proteins.

101 Results

102 LC-MS Proteomics to characterize the BR-body proteome

103 In order to define the *C. crescentus* BR-body associated proteome, BR-body enrichment was
104 performed as in[30] and subjected to bottom-up proteomics preparation and analysis (Fig 1A). Here we
105 compared enriched BR-body samples to a mock treated lysate using a mutant that is unable to assemble
106 BR-bodies due to the deletion of the C-terminal IDR of RNase E[30]. 100 μg protein was prepared in
107 triplicate for either condition and converted into peptides via enzymatic digestion using S-Traps[32]. Each
108 sample was analyzed by LC-MS/MS in technical triplicate. Peptide-spectral matching, protein inference
109 and Label Free Quantification (LFQ) was performed using FlashLFQ in MetaMorpheus[33]. Data were
110 filtered to an FDR of 1.0% and exported as text for analysis. Using these parameters, a total of 1079
111 proteins were identified in both samples, and the ratio of signal in the BR-body enriched sample (JS299)
112 over the negative control (JS221) was plotted (Fig 1B). 111 proteins were identified to be enriched in
113 BR-bodies. These enriched proteins had Log2 BR-body enrichment value of >1 (>2-fold enrichment) with
114 a >95% confidence interval (resulting p-values subject to Benjamini-Hochberg correction) or were
115 identified in all three biological replicates in BR-body enriched samples but were not detected in the
116 negative control. These enriched proteins were predominantly cytoplasmic, while proteins derived from
117 other cellular compartments were depleted, suggesting reasonable enrichment of BR-bodies occurred in
118 the sample. In addition, we observed significantly higher scores for known RNase E associated proteins,
119 while proteins that interact with polar biomolecular condensates were highly depleted (Fig 1B),
120 suggesting that the enrichment is likely not contaminated with all cellular condensates. Of all the
121 enriched proteins, go-term enrichment found proteins with RNA binding, ATP binding, GTPase activity,
122 or RNA degradation functionalities (Fig 1B). To validate whether BR-body enriched proteins localize into
123 BR-bodies *in vivo*, we expressed a set of YFP-tagged proteins that were enriched in BR-bodies together
124 with a set of other RNA related proteins that were not enriched in BR-bodies from the vanillate locus
125 (Fig S1) and determined the average number of foci/cell (Fig 1C). Interestingly, 7/11 proteins from the

126 BR-body enriched set assembled into foci in the cells, while only 3/11 proteins from the negative control
127 set showed foci. Amongst the 4 known BR-body clients we found that 3/4 were enriched within these
128 assemblies. RNase D1 was found to be RNase E associated[34] and showed foci within cells, however, was
129 depleted in the BR-body proteomics data. Of the 4/11 proteins that were enriched but did not form
130 foci, it is possible that the C-terminal YFP tag might interfere with their ability to form foci, as SmpB
131 which was found to form foci by immunofluorescence[35] and did not form foci when fused to YFP.
132 Interestingly, MetK has been found to form foci previously[36] and RNase HI may be associated with the
133 replisome foci, so both of these foci are unlikely to be BR-bodies, and likely represent other structures.
134 Overall, the larger abundance of foci in the BR-body enriched set suggest the BR-body enriched
135 proteomic data represents many true-positive BR-body associated proteins with limited false-positives.

136 Identification of BR-body associated scaffolds that condense independent of RNase E

137 Since the C-terminal IDR of RNase E was found to be necessary and sufficient to form BR-bodies,
138 we tested whether RNase E was required for BR-body enriched proteins to form foci (Fig 2). Since RNase
139 E is essential, we used an RNase E depletion strain where the sole copy of RNase E is under control of
140 the xylose promoter[4]. While most proteins maintained similar YFP fluorescence, RhlB, Aconitase,
141 PNPase, and RNase H1-YFP proteins were expressed at levels that were too low to detect in the
142 depletion strain. To overcome low expression for aconitase, we utilized a different strain in the lab used
143 previously in which Aconitase-YFP was present at its native loci in the same xylose dependent RNase E
144 depletion strain[4]. We observed and quantified foci for each of the YFP fusions, however, RNase D1
145 appeared to show localization to the inner membrane with a lower number of foci as compared to the
146 other strains tested. For Aconitase, RNase D1, Hfq, and Rho, fluorescent foci levels dropped significantly
147 upon RNase E depletion, suggesting that these proteins likely require RNase E to assemble into foci.
148 Interestingly, for MetK and RhlE, foci levels were similar or higher upon RNase E depletion, suggesting
149 that these two proteins assemble into foci independent of RNase E.

150 As MetK and RhlE proteins were identified to assemble RNase E independent foci *in vivo*, we
151 tested whether these proteins could directly self-assemble into condensates *in vitro*. In addition to MetK
152 and RhlE, we also included several additional proteins from the BR-body enrichment dataset or which
153 were known to interact with RNase E (Figs 3, S2A). Each protein was incubated near their estimated *in*
154 *vivo* concentration[37], and was incubated with or without 20 ng/µL of *C. crescentus* total RNA. We
155 identified that RhlE, DeaD, Hfq, MetK, and FabG all assembled RNA stimulated condensates *in vitro* (Figs
156 3A, B), suggesting that these proteins are scaffolds that can drive RNA dependent condensation.
157 Conversely, a majority of the proteins tested including PNPase, Aconitase, RhlB, RNase D1, ribosomal
158 protein S1, NudC, RppH, Rho, NusG, DnaK, and tyrosyl tRNA synthetase (TyrRS) did not undergo phase
159 separation regardless of the presence of RNA (Fig S2B). Consistent with the phase-separation of RhlE,
160 DeaD, and Hfq, the homologous proteins from *E. coli* were recently found to assemble into condensates
161 *in vitro* or when overexpressed *in vivo*[7,38]. To test whether these structures are condensates, we
162 performed high-salt and RNase treatment (Fig 3C), and in each case all the structures were strongly
163 dissociated, suggesting multivalent electrostatic interactions with RNA are likely important for driving
164 phase separation, like in RNase E condensates[4]. RhlE, DeaD, and Hfq contain intrinsically disordered
165 regions (IDRs) (Fig 3A) that have been characterized as important for their *E. coli* homologues to be able
166 to form droplets[38,39]. Prior experiments also showed that the IDR of RNase E was both necessary and
167 sufficient for phase separation[4]. To test the function of these IDRs on phase-separation we deleted the
168 IDRs of *C. crescentus* RhlE, DeaD, and Hfq and tested for their ability to phase-separate and found that

169 for Hfq and DeaD the IDR deletions showed reduced phase-separation, while for RhlE the IDR deletion
170 was indistinguishable from wild-type (Fig S2C). We did not include FabG and MetK in these experiments
171 as no disordered regions were predicted in their sequences (Fig 3A). Overall, this suggests that for some
172 of these scaffold proteins, IDRs provide a positive influence of phase separation, but are not strictly
173 required for phase separation.

174 A complex network of molecular interactions regulates RNP condensate

175 To better understand which proteins can enter BR-bodies, we selected a set of 18 proteins (Fig
176 S2A) to test further for their recruitment directly into RNase E droplets (Fig 4A). We picked proteins
177 enriched from the BR-body proteomics dataset with known RNA-processing roles, proteins known to
178 have protein-protein interactions with RNase E but not detected in the BR-body proteomics experiment,
179 as well as negative control proteins with low BR-body enrichment and no known/predicted interaction.
180 In these experiments RNase E and RNA were added to form an RNase E condensate, followed by the
181 incubation of a Cy5 labeled test protein. The partition coefficient was calculated from the images for
182 each protein assayed based on the Cy5 fluorescence (Figs 4B, S4A). Here we observed that the core RNA
183 degradosome proteins PNPase, Aconitase, RhlB, and RNase D1 all had positive partition coefficients
184 ranging from 2.7 to 4.7 showing they enter RNase E condensates, while our negative controls of BSA or,
185 SpmX which forms a polar signaling condensate[6], did not enter and yielded a partition coefficient near 1
186 indicating no enrichment. We also identified partition coefficients at similar levels to the core
187 degradosome proteins for RhlE, DnaK, and FabG. In contrast NudC, RppH, Rho, NusG, and TyrRS all
188 contained partition coefficients close to 1, similar to the negative control BSA and SpmX (Fig 4B). The
189 low partition coefficients for RppH and NudC are consistent with their lack of enrichment in the BR-body
190 proteomics assay, however, Rho, NusG, and TyrRS all had significant enrichment in the BR-body
191 proteomics data suggesting they may enter BR-bodies indirectly through another protein. Despite the
192 finding that many proteins were able to enter BR-bodies, none of these proteins altered the partition
193 coefficient of RNase E (Fig S3B), suggesting that a majority of BR-body associated proteins are not
194 dramatically influencing RNase E's condensation.

195 As some BR-body proteins were found to assemble into RNA dependent condensates on their
196 own, we tested which BR-body associated proteins might induce condensation in the absence of RNA
197 (Fig S4). To test each client's ability to stimulate RNase E condensation, we added each protein at their
198 in-vivo concentration[37]. Interestingly, we found that PNPase, RhlB, and RhlE stimulated RNase E
199 condensates rather robustly in the absence of RNA (Fig S4A). In addition, FabG and Hfq stimulated
200 irregularly shaped condensates in the absence of RNA while Aconitase, RNase D1, NudC, RppH, Rho,
201 NusG, DnaK, TyrRS, ribosomal protein S1, and MetK did not stimulate RNase E condensation (Fig S4A).
202 This suggests that a subset of BR-body associated proteins can stimulate condensation independent of
203 RNA.

204 Interestingly, we observed that the addition of ribosomal protein S1 (RpsA) or MetK, which were
205 not BR-body enriched (Table S1) but were previously found to associate with RNase E via CoIP[40], could
206 dissolve RNase E droplets *in vitro* (Figs 4A,5A). Ribosomal protein S1 could only dissociate the droplets if
207 the condensates contained total RNA, while MetK showed strong dissolution if RNase E was condensed
208 with RNA or with the protein PNPase. To test whether the differences between S1 and MetK were
209 related to their inherent RNA binding interactions, we examine the apparent binding on 9s rRNA, a
210 known RNase E substrate[31]. Based on the native gel shifts we found that ribosomal protein S1 bound

211 RNA with tighter apparent affinity than MetK (Fig 5B). The tighter apparent affinity with RNA may
212 explain why ribosomal protein S1 preferentially dissolves RNase E condensates in the presence of RNA.
213 We also used a coIP assay with MBP-RNase E to test MetK and ribosomal protein S1 association with
214 MBP-RNase E. Indeed, as compared to the core BR-body protein aconitase which is thought to
215 stoichiometrically bind to RNase E[30], we found that both ribosomal protein S1 and MetK showed lower
216 CoIP than aconitase. However, MetK showed a faint band of protein retained on the resin, while
217 ribosomal protein S1 showed no detectable retention (Fig 5C). Overall, these data suggest that MetK
218 dissociates BR-bodies through interactions with the RNase E protein (Fig 5). To examine whether this
219 observed *in vitro* dissolution effect is relevant *in vivo*, we inserted the ribosomal protein S1 and *metK*
220 genes into the pBXMCS-2 overexpression vector[41] and transformed the plasmid into a strain harboring a
221 tagged BR-body marker (Aconitase-mCherry)[4]. We observed *in vivo* that both MetK and ribosomal
222 protein S1 overexpression strongly reduced Aconitase-mCherry foci (Fig 5D), confirming that their
223 dissolution of BR-bodies observed *in vitro* can also occur *in vivo*.

224 As some BR-body enriched proteins were able to assemble into RNP condensates independent
225 of RNase E (Fig 4B), the client specificity of these RNP condensates was unknown. As the RNA
226 degradosome client proteins are known to be stoichiometrically bound to RNase E via direct protein-
227 protein interaction sites[31,40], we tested the specificity of each driver/scaffold to each core RNA
228 degradosome protein labeled with Cy5 dye (Fig 6A). Here we observed a larger partition coefficient for
229 all Cy5 degradosome clients to RNase E condensates as compared to any of the other scaffolds/drivers
230 (Figs 6A, S4B), suggesting that the degradosome proteins have a specificity for RNase E condensates,
231 likely through their protein-protein interactions.

232 Next, the miscibility of the scaffolds/drivers of each single RNP condensate was examined (Fig 6B).
233 First, we pre-formed a condensate using an unlabeled scaffold and then added in a Cy5 labeled scaffold
234 in all pairwise combinations and assayed the partition coefficients. We induced condensation in the
235 presence or absence of RNA to test the RNA dependency of each interaction. In the presence of RNA we
236 assayed condensate formation using the predicted *in vivo* protein concentrations[37], and in the absence
237 of RNA condensates were stimulated by increasing the protein concentration above its *in vivo*
238 concentration. For the RNase E condensate, we observed similar recruitment of other scaffolds
239 regardless of whether the condensates were formed with RNA or protein only (Figs 6B, S4B). The
240 partition coefficients for these scaffolds into RNase E condensates tracked with the BR-body enrichment
241 measured previously. RhlE was recruited strongest into the RNase E condensate (11 partition
242 coefficient) and had the highest observed BR-body enrichment (10 fold), while Hfq (7.5 partition
243 coefficient, 3.2 BR-body enrichment), FabG (3.8 partition coefficient, 2.2 fold BR-body enrichment), and
244 DeaD (1.5 partition coefficient, 1.6 fold BR-body enrichment). For RhlE, we observed that it was
245 recruited strongly into other RNP condensates, with partition coefficients ranging from 4.3 to 11, while
246 the other scaffolds were recruited poorly into RhlE-RNA condensates, with partition coefficients ranging
247 from 1.5 to 2.5. In the absence of RNA, RhlE strongly recruited RNase E (12) or DeaD (9.8) while Hfq and
248 FabG maintained similar partition coefficients (Fig S4B). DEAD condensates showed strong recruitment
249 of RhlE and lower recruitment of the other scaffolds, with subtle changes in the presence or absence of
250 RNA. While RhlE and FabG were similarly recruited to Hfq condensates regardless of the presence of
251 RNA, RNase E dissolved Hfq-RNA condensates while Hfq protein only condensates strongly recruited
252 RNase E (6.9 partition coefficient) while DEAD was recruited at a low level in Hfq-RNA condensates (1.8
253 partition coefficient) and dissolved Hfq only condensates. FabG condensates only formed in the

254 presence of RNA and showed strongest recruitment of RhlE (7.4) and Hfq (3.4). In summary, the scaffold
255 proteins which assemble diverse RNP condensates show specificity of recruitment, suggesting that some
256 RNP condensates can intermix, while others likely do not.

257 The asymmetric recruitment/dissolution (Fig 6B) and specificity of clients (Fig 6A) observed may
258 help shape the composition of heterogeneous RNP condensates in the cell. We chose to study RhlE-
259 RNase E pair further because it showed the strongest directional recruitment in the presence of RNA (Fig
260 6B). First, we altered the order of addition of RhlE and RNase E in which we could either mix both
261 proteins together before triggering phase separation (Fig 6C). If the proteins are mixed before
262 condensation with RNA, we observed that RNase E and RhlE mix uniformly. We also changed the order
263 of addition and pre-assembled each protein into condensates with RNA before mixing both RNP
264 condensates together (Fig 6C). When each protein was pre-assembled into a condensate, we observed
265 that RNase E and RhlE condensates did not readily mix with each other. This contrasts with the prior
266 observation that free RhlE readily entered RNase E condensates (Fig 6B), suggesting that the order of
267 assembly influences the composition of these RNase E and RhlE condensates.

268 To test whether RhlE forms condensates separate from BR-bodies *in vivo*, we coexpressed RhlE-
269 YFP together with Aconitase-mCherry (a marker for BR-bodies) and imaged them in the same cells (Fig
270 6D). As a control, we imaged RNase E-YFP together with Aconitase-mCherry, which are known to
271 strongly colocalize[4]. In general, we observed a heterogeneous mixture of RhlE foci, RNase E foci, and
272 mixed RhlE/RNase E foci. For each YFP focus we observed, we drew line traces and calculated the
273 Pearson correlation between the YFP and mCherry channels across the line trace. The RNase E signal
274 was strongly colocalized with Aconitase-mCherry (R=0.9), and for a strain lacking YFP, we found that the
275 correlation between YFP autofluorescence and Aconitase-mCherry was near zero. Interestingly, we
276 observed that RhlE and Aconitrase had an intermediate correlation (R=0.4), with some RhlE foci strongly
277 correlating with Aconitase, and other RhlE foci totally lacking Aconitase (Fig 6D). In addition to
278 colocalization, we also examined the assembly order of RNase E and RhlE condensates formation *in vivo*
279 with taking time-lapse movies of cells. To do this, we took time-lapse movies of cells and examined the
280 order of RhlE and RNase E foci formation in cells. As a positive control, we observed that RNase E-YFP
281 and Aconitase-mCherry foci appear simultaneously (Fig 6E, S5A). When BR-bodies appear first, as
282 indicated by Aconitase-mCherry foci, we consistently observed RhlE-YFP signal within these foci (Fig 6E),
283 consistent with the ability of RNase E condensates to recruit RhlE *in vitr*o (Fig 6B). In contrast, RhlE-YFP
284 foci that appeared first generally lacked a colocalized Aconitase-mCherry focus, also consistent with the
285 lack of *in vitro* recruitment (Fig 6B). Taken altogether, these observations suggest that the network of
286 interactions driving RhlE and RNase E condensation likely controls the ability of these condensates to
287 coassemble and mix both *in vitro* and *in vivo*. To further test how the network of interactions affects the
288 condensates, we performed *in vitro* FRAP on RhlE and RNase E droplets (Fig S5B). We observed that
289 RNase E rapidly recovers either in RNase E-RNA condensates or in mixed RNase E-RhlE-RNA
290 condensates, while RhlE showed little to no recovery in RhlE-RNA condensates or RNase E-RhlE-RNA
291 condensates (Fig S5B). To test whether RhlE ATPase activity might influence its dynamics, we found the
292 addition of ATP-Mg^{2+} did not alleviate RhlE recovery (Fig S5B). Overall, this suggests that the material
293 properties of RhlE-RNA and RNase E-RNA condensates contribute to the unidirectional mixing observed
294 *in vitro* and *in vivo*.

295 As RNase E did not appear to readily enter other associated RNP condensates (Fig 6A), we
296 wanted to better understand the role of RNA and the associated degradosome proteins on its

297 condensation. We therefore examined the kinetics of condensation via time-lapse microscopy (Fig 7A,
298 7B). This assay likely reflects the kinetic processes of phase-separation and surface wetting of the
299 microscope slide. When incubated alone at its predicted *in vivo* concentration, RNase E did not phase
300 separate *in vitro* even after long incubations of several minutes. RNase E was able to phase separate
301 without RNA after prolonged incubation of many minutes, and at concentrations much higher than its
302 predicted *in vivo* concentration the extent of phase separation was enhanced (Fig S6). The addition of
303 RNA strongly stimulated the rate of condensation, occurring on the sub-minutes timescale, consistent
304 with the known importance of RNA for condensation *in vivo* and in end-point *in vitro* assays[4,29].
305 Importantly though, RNase E is known to scaffold the RNA degradosome protein complex, and the
306 degradosome proteins stoichiometrically bind to RNase E[31] and are homogeneously present with RNase
307 E in BR-bodies[4]. To test the effects of degradosome proteins on condensation kinetics, we added either
308 PNPase or the full set of core degradosome proteins (PNPase, Aconitase, RhlB, and RNase D1) to the
309 condensation assembly experiment. The addition of PNPase or the full set of core RNA degradosome
310 proteins still allowed for rapid RNA stimulated condensation on the sub-minute timescale. This suggests
311 that the combined interactions with the RNA degradosome proteins likely do not dramatically alter
312 RNase E's condensation kinetics in the presence of RNA. This may be due to the degradosome protein
313 binding sites being located outside the Arg-rich RNA binding sites in the C-terminal domain[31]. As noted
314 previously, we observed that the degradosome protein PNPase was able to stimulate RNase E
315 condensation *in vitro* in the absence of RNA (Fig S4A). We therefore assayed the kinetics of RNase E
316 PNPase condensation in the absence of RNA and found that the kinetics were dramatically slower than
317 in the presence of RNA. Overall, this suggests that RNA provides the strongest stimulation in
318 condensation, and the RNA degradosome clients can provide a slight further enhancement in RNA-
319 mediated condensation.

320 To understand if RNA or degradosome protein interactions alter the mobility of molecules in the
321 condensed state, we performed FRAP experiments (Fig 7C). RNase E condensates lacking RNA had the
322 slowest recovery, at 2.4 min $\tau_{1/2}$, while the addition of RNA accelerated the FRAP recovery $\tau_{1/2}$to 0.23
323 [27]min. Interestingly, the addition of PNPase and RNA, or all degradosome proteins and RNA showed fast
324 mobility between 0.34 and 0.42 min $\tau_{1/2}$, similar to the RNase E with RNA sample. This suggests that the
325 addition of RNA significantly increases the mobility of RNase E condensates, regardless of the presence
326 of degradosome clients. Interestingly, the addition of RNase E and PNPase in the absence of RNA
327 showed a recovery $\tau_{1/2}$of 0.38 min. This suggests that even though the degradosome proteins don't
328 dramatically stimulate the rate of condensation, the degradosome protein interactions likely do
329 influence the mobility of RNase E within the droplets, either indirectly through altering the structure of
330 the CTD or directly by influencing the multivalent protein-protein interactions in the condensed state.
331 Altogether, RNA appears to stimulate the rate of RNase E condensation, while the recruitment of RNA or
332 protein clients helps to increase the mobility of RNase E within the condensate which may help promote
333 enhanced biochemical activity.

334 Discussion

335 **A complex protein interaction network impacts BR-body condensation and composition**

336 BR-body proteomics revealed >100 different proteins of various biochemical functions are enriched,
337 suggesting they are more complex than previously assumed. Importantly, many other scaffolds that can
338 undergo heterotypic phase separation with RNA are also enriched in BR-bodies, which suggests that

339 many cellular RNP condensates exist and interact with BR-bodies. Five proteins which interact with
340 RNase E were identified as scaffolds that can phase separate with RNA *in vitro*, including RhlE, DeaD,
341 Hfq, FabG, and MetK. Together with RNApol condensates identified previously[5], this suggests that
342 bacteria contain many RNP condensates likely help coordinate multi-step reactions in RNA processing[3].
343 As observed for yeast P-bodies, a set of "core" proteins were found to be quantitatively enriched[27] and
344 likely homogeneously represented in these structures, were successfully reconstituted *in vitro* with
345 similar dynamics properties and stoichiometries identified[28]. We observed that a subset of BR-body
346 enriched proteins known to stoichiometrically assemble the RNA degradosome (RNase E, RhlB,
347 Aconitase, and PNPase), appear to be uniformly enriched in BR-bodies *in vivo*[4] and selectively recruited
348 to RNase E condensates *in vitro* (Fig 6). This suggests that the RNA degradosome likely composes the
349 "core" set of proteins making up each BR-body. An important goal working forward will be to define the
350 role of BR-body localization to each of the core enzymes involved in the RNA decay process. Indeed, by
351 using a two protein BR-body system using only RNase E and PNPase, PNPase activity was observed to be
352 directly stimulated via condensation with RNase E[17], suggesting organization in BR-bodies may help to
353 stimulate RNA degradosome activity. By testing the full complement of "core" BR-body proteins and also
354 the set of "accessory" BR-body associated proteins, we will likely be able to delineate the normal vs
355 specialized functions of BR-bodies.

356 As DEAD box RNA helicases appear to be important players in biomolecular condensates[38,42], we
357 observed that RhlE and DeaD act as scaffolds that undergo RNA dependent phase-separation *in vitro*,
358 while RhlB did not, similar to what was observed for their *E. coli* homologues[38], suggesting phase
359 separation is a conserved feature of these proteins. Interestingly, we observed strong recruitment of
360 RhlE and RhlB into RNase E condensates, while DeaD was observed to be recruited to a lower extent (Fig
361 4). While RhlB foci were dissociated in cells after RNase E depletion and showed strongly correlated
362 localization with RNase E[4], RhlE remained localized in foci even after RNase E depletion and showed
363 heterogenous partially overlapping localization with RNase E (Fig 2). Taken together, this suggests all
364 BR-bodies likely contain RhlB, a core part of the RNA degradosome, while the heterogeneity of RhlE
365 colocalization suggests that some BR-bodies lack this protein. The function of DEAD box proteins in BR-
366 bodies is not well understood, however, RhlE becomes more highly expressed when *C. crescentus* is
367 grown in the cold[40] which may alter the composition and function of BR-bodies in these conditions.

368 As the BR-body transcriptome previously revealed that poorly translated mRNAs and small RNAs
369 were highly enriched substrates, the BR-body proteomics identified Hfq as a BR-body enriched protein.
370 Interestingly, the protein Hfq which is known to chaperone small RNAs to base-pair to their target
371 mRNAs and repress translation/induce decay[43–47], was found to be enriched in BR-bodies, to form foci in
372 *C. crescentus*, and to phase separate with RNA *in vitro*. *E. coli* Hfq was recently found to phase separate
373 with DNA ,polyphosphate[39], and RNA[10], and its condensation is promoted *in vitro* by its intrinsically
374 disordered CTD[39]. Interestingly, *E. coli* Hfq foci were previously identified to colocalize with RNase E in
375 Nitrogen starved *E. coli* cells[7], and while Hfq is not a core member of the *E. coli* or *C. crescentus* RNA
376 degradosome, it has been found to associate with RNase E in multiple species[48]. Interestingly, we
377 observed that *C. crescentus* Hfq is readily recruited into RNase E-RNA condensates, but RNase E was not
378 recruited into Hfq-RNA condensates, suggesting directionality in forming a mixed condensate. *E. coli*
379 Hfq condensates were found to promote sRNA-mRNA annealing[10] and RNase E IDR mutants that prevent
380 BR-body phase separation were found to prevent sRNA-mRNA silencing[49]. Therefore the coordination of

381 Hfq with BR-bodies likely helps to degrade translationally repressed mRNAs as has been proposed for
382 miRNA/siRNA/lsm enrichment in P-bodies[22].

383 The identification of BR-body associated proteins which can dissolve BR-bodies (ribosomal protein
384 S1 and MetK) suggests they may play important regulatory roles in controlling BR-body assembly.
385 Ribosomal protein S1 appears to dissolve RNase E condensates via its RNA binding capacity, while MetK
386 appears to dissolve RNase E via protein-protein interaction with RNase E (Fig 5). Ribosomal protein S1 is
387 present in a ribosome bound and a ribosome free form where it is known to unfolds structured mRNAs
388 in preparation for translation initiation[50], and protect mRNAs from RNase E dependent decay[51]. Since
389 BR-bodies and ribosomes compete for mRNA substrates[4], ribosomal protein S1 may prevent BR-body
390 condensation on highly translated mRNAs by locally disrupting RNase E condensation when in
391 polysomes. Alternatively, if ribosomal protein S1 dissociates from the ribosome, it may be able to
392 globally dissolve BR-bodies, potentially acting as a sensor of translation. MetK an essential enzyme in
393 which generates S-adenosyl-methionine and which we identified could assemble RNP condensates.
394 While it was identified as an RNase E binding protein from CoIP in cells grown in the cold, we identified a
395 weak *in vitro* CoIP of RNase E and MetK proteins (Fig 5), suggesting MetK likely inhibits RNase E
396 condensation directly from blocking multivalent interactions, or indirectly by altering the conformation
397 of RNase E. Despite its rather weak RNA binding observed *in vitro*, MetK from *C. crescentus* phase
398 separated in the presence of RNA, and homologs from *S. meliloti* and *E. coli* were identified to bind
399 RNA[52]. Since MetK is the sole enzyme creating SAM in *C. crescentus*, perhaps it might act as a metabolic
400 sensor that could tune the number of BR-bodies to Carbon availability. In line with this hypothesis, its
401 levels are dramatically altered upon Carbon starvation[53].

402 **Critical importance of RNA in bacterial RNP body condensation**

403 Excitingly, reconstitution of minimal BR-body cores revealed that RNA, which was hypothesized
404 to play a key role in BR-body assembly *in vivo*[4], also plays a key role in BR-body assembly *in vitro*. We
405 observed that RNA can kinetically stimulate the rate of BR-body condensation on the sub-minutes
406 timescale (Fig 7), further suggesting rifampicin-induced RNA depletion is likely the main cause of RNase
407 E's robust foci dissolution and not other cellular perturbations from this drug (such as nucleoid
408 expansion[54]). The addition of RNA degradosome proteins does not alter the rate of RNase E
409 condensation, however, does appear to enhance RNase E mobility by FRAP (Fig 7). Based on BR-body
410 transcriptomics, these structures are mostly enriched for long poorly translated mRNAs and small RNAs
411 and depleted of rRNA and other highly structured ncRNAs[29]. This suggests that at least under
412 logarithmic growth conditions, availability of poorly translated RNA helps catalyze rapid BR-body
413 assembly. Interestingly, BR-bodies could be induced with some client proteins in the absence of RNA,
414 such as PNPase, however, the rate of the condensation was far slower than in the presence of RNA.
415 While likely not relevant under log phase growth conditions as BR-bodies were observed to have sub-
416 minutes dynamics[4], such assemblies might occur under non-growing conditions, like stationary phase.

417 The identification of five new RNP condensates associated with BR-bodies suggests these
418 structures likely have a broader role in bacterial cell organization than previously anticipated. Indeed,
419 recent high-throughput methods designed to detect proteins crosslinked to RNA identified >1100 RNA
420 binding proteins in *E. coli* including many metabolic enzymes[55,56]. Indeed, we identified two metabolic
421 enzymes, MetK and FabG, which have the capacity to phase separate with RNA (Fig 3). While the ability
422 of metabolic enzymes to bind to RNA is referred to as "moonlighting" RNA binding activity[57], it's possible

423 that due to large number of RNA binders RNP condensates plays a broad role in organizing metabolic
424 pathways in the bacterial cytoplasm. While experimentation to identify and characterize new
425 condensates is slow, bioinformatic prediction of proteins that can undergo phase separation is making
426 progress, however, even next generation algorithms do not accurately predict the phase separation of
427 all five of these proteins. Perhaps current phase separation prediction algorithms rely too much on IDR
428 predictions, which appear to often affect phase separation, but are not always required[58]. In developing
429 next generation algorithms to predict phase separation, it will be important for the training data sets to
430 include bacterial phase separating proteins so we can begin to make accurate estimates for the fraction
431 of the bacterial proteome that is able to phase separate.

432 **Materials and Methods**

433 ***Caulobacter crescentus* cell growth**

434 All *C. crescentus* strains used in this study were derived from the wild-type strain NA1000[59], and were
435 grown at 28˚C in peptone-yeast extract (PYE) medium or M2 minimal medium supplemented with 0.2%
436 D-glucose (M2G)[60]. When appropriate, the indicated concentration of vanillate (500 mM), xylose (0.2%),
437 gentamycin (Gent) (0.5 mg/mL), kanamycin (Kan) (5 mg/mL), spectinomycin (Spec) (25 mg/mL), and/or
438 streptomycin (Strp) (5 mg/mL) was added. Strains were analyzed at mid-exponential phase of growth
439 (OD 0.3-0.6). Optical density was measured at 600 nm in a cuvette using a Nanodrop 2000C
440 spectrophotometer.

441 **BR-body enrichment assay and LC-MS proteomics**

442 BR-body enrichment was performed as in[30]. Enriched BR-bodies were then resuspended in buffered SDS
443 before proteomics sample preparation.

444 *Suspension Trapping (S-Trap) Sample Preparation:*

445 100 µg protein lysate (JS221 or JS299) was prepared in triplicate according to the manufacturer's
446 instructions. Trypsin was resuspended in a 50 mM ABC buffer and added to S-Traps at a 1:50
447 (enzyme:protein w/w) ratio and incubated for 8 hours at 37˚C. After the digestion, peptides were eluted
448 according to the manufacturer's protocol and vacuum centrifuged to dryness prior to desalting.

449 *Solid Phase Extraction (SPE):*

450 All samples were desalted prior to MS analysis with 10mg HLB cartridges according to manufacturer's
451 instructions as in [61]. Samples were dried prior to analysis and stored at -80˚C until re-suspension for LC-
452 MS/MS.

453 *Analysis via nano UHPLC-MS/MS:*

454 Dried digests were resuspended in 0.1% formic acid in water to a concentration of 250 ng/µL. 2 µL of
455 solution was injected onto a 100mm x 100µm C_{18} BEH reverse phase chromatography column with an
456 autosampler (nanoACQUITY, Waters Corporation). Peptides were separated over a 95 minute
457 segmented gradient from 4-35% B (A= H_2O + 0.1% FA, B=acetonitrile + 0.1% FA) MS-MS/MS was
458 performed on a Q-Exactive HF mass spectrometer via electrospray ionization (Thermo Fisher Scientific).
459 Samples were collected in biological triplicate, and data was acquired in technical triplicate injections
460 using a TOP17 data-dependent method (DDA).

461 *Peptide-Spectrum Matching (PSM):*

462 RAW files from technical and biological triplicates were processed for peptide identification, protein
463 inference, and false-discovery rate using the MetaMorpheus search engine[62]. A *C. crescentus* FASTA
464 from UniProt (proteome ID UP000001364) was used with a common contaminant file. Data were first
465 calibrated prior to search ('Traditional') using the default parameters. For 'Main' search, additional
466 parameters included a maximum of two missed cleavages, two variable modifications per peptide, and a
467 minimum peptide length of seven amino acids. The precursor mass tolerance was set to 5 ppm and the
468 product mass tolerance was set to 20 ppm. The 'common' fixed and 'common' variable modifications
469 were selected, and identifications were filtered to a q-value of <0.01. RAW data files are available
470 through MassIVE with accession number (MSV000090894).

471 ***In vivo* localization of BR-body associated proteins**

472 All *C. crescentus* protein fusion strains were grown in PYE-Kan or PYE-Gent media overnight. The next
473 day, from the log-phase cultures, a few dilutions were done in M2G media containing appropriate
474 amount of Kan or Gent and grown for overnight. The next day, the mid log-phase cultures were induced
475 with 500 mM vanillate and grown for 6 hours. 1µL of the cells were spotted on a M2G 1.5% agarose pad
476 and imaged using a YFP filter cube.

477 **RNase E depletion**

478 Depletion strains containing the xylose inducible copy of RNase E were first grown overnight in M2G-
479 Kan-Gent media containing 0.2% xylose. The next day, from the log-phase cultures, a few dilutions were
480 done in M2G-Kan-Gent media containing 0.2% xylose overnight. Mid-log phase cells were then washed 3
481 times with 1 mL growth media and resuspended in growth media and split into two tubes and one
482 treated with 0.2% xylose. Depletion strains were analyzed at mid-exponential phase of growth (OD 0.3-
483 0.6) and after 24 hours of depletion of xylose. 1 µL of the cells under each condition was spotted on a
484 M2G 1.5% agarose pad and imaged using a YFP filter cube.

485 **Colocalization of YFP tagged proteins with BR-body marker Aconitase-mCherry**

486 Dual-labeled strains expressing YFP tagged proteins with BR-body marker Aconitase-mCherry were first
487 grown overnight in PYE-Kan-Spec-Strp media in 3 dilutions. Mid log-phase cells were split into two tubes,
488 and one was treated with 0.02% xylose and grown for 3.5 hours. 1 µL of the cells under each condition
489 was spotted on a M2G 1.5% agarose pad and imaged using YFP and TX-Red filter cubes. Fluorescence
490 level analysis of the droplets was performed using MicrobeJ[63]. The correlation analysis was performed
491 in Microsoft Excel.

492 **Dissolution of MetK and ribosomal protein S1**

493 Strains expressing MetK and ribosomal protein S1 with BR-body marker Aconitase-mCherry were first
494 grown overnight in PYE-Kan-Spec-Strp media in 3 dilutions. Mid log-phase cells were split into two tubes,
495 and one was treated with 0.2% xylose and grown for 6 hours. 1 µL of the cells under each condition was
496 spotted on a M2G 1.5% agarose pad and imaged using TX-Red filter cubes.

497 **Cell imaging**

498 Around 1 µL of cells were immobilized on 1.5% agarose pads made with M2G medium on microscope
499 slides (Thermo SCIENTIFIC 3051), air dried and imaged with immersion oil on a coverslip. All images were
500 collected using a Nikon Eclipse NI-E with CoolSNAP MYO-CCD camera and 100x Oil CFI Plan Fluor (Nikon)
501 objective, driven by Nikon elements software. The filter sets used for YFP, CFP and mCherry imaging
502 were chroma 96363, 96361, and 96322 models respectively. Cell image analysis was performed using
503 Microbe-J[63].

504

505 **QUANTIFICATION AND STATISTICAL ANALYSIS**

506 **Foci quantification**

507 *In vivo* protein fusion foci were quantified using Microbe J[63]. Cell outlines were first identified using the
508 medial axis algorithm in the phase channel with minimal cell length of 1.35 µm and the segmentation
509 option. Cell outlines were then manually curated to remove cells containing erroneous outlines. Next,
510 the maxima function was used with ''foci'' option with minimal area of 0.01 μm^2 and minimal length of
511 0.1 µm with the segmentation option on and the association inside option on. Tolerance and Z-score
512 parameters tuned for each protein fusion type.

513 To quantify the average foci per cell of each strain, three replicates were performed in three different
514 days and 3 images were analyzed from each day. We summed all foci identified in each cell, divided by
515 the total of the cell to calculate number of foci per cell.

516 **RNA extraction**

517 For RNA extraction mid-log phase cells (0.3 to 0.5 OD600) were pelleted at 20,000 g for 10 minutes in a
518 microcentrifuge. Then, cells were resuspended in 1mL 65˚C Trizol (1mL for each 1 mL of NA1000 cell)
519 and incubated at 65˚C for 10 min in a heat block. 200mL of chloroform was added and incubated for 5
520 min at room temperature. The samples were then spun at max speed (20,000 g) in a microcentrifuge for
521 10 min at room temperature. The aqueous layer was removed and RNA samples were precipitated using
522 700 mL isopropanol at -80˚C for 1 hour and spun at 20,000 g for 1 hour at 4˚C. The supernatant was
523 removed and the pellet was washed with 1 mL of 70% ethanol. The samples were then spun again for 10
524 min at 20,000 g at 4˚C, the supernatant was removed, and the pellet was resuspended in RNase-free
525 water. RNA samples were run on 1X TBE/7M Urea denaturing PAGE gels and visualized with SYBR-Gold
526 nucleic acid gel stain.

527 **Protein purifications:**

528 The protein coding genes were cloned into pET His6 MBP TEV or pET His6 G TEV or pET28a plasmids and
529 the expressed proteins are purified by His tag affinity purification followed by the removal of MBP or G
530 tag by TEV proteolysis. RNase E CTD, RhlB, RhlE -IDR were expressed as N-terminal MBP fusions, all the
531 other proteins were expressed as N-terminal G protein fusions. Briefly, the proteins are expressed in
532 BL21 DE3 cells by inducing with 0.5mM IPTG at 37° C for 3.5 hours in 2X Luria-Bertani media, and the
533 cells pelleted at 5000 rpm for 20 minutes were lysed in a lysis buffer (20mM Tris pH 7.4, 500mM NaCl,
534 10% Glycerol, 10mM Imidazole, 1mM PMSF, 1 tablet protease inhibitor cocktail and DNase I) at 4° C
535 using a sonicator with 10 seconds pulse on and 30 seconds pulse off times for 18 cycles. The lysed cells
536 were centrifuged at 15000 rpm for 45 minutes and the resultant supernatant was loaded onto
537 equilibrated Ni-NTA resin, the protein bound resin was washed with 10 column volumes each of lysis

538 buffer, chaperone buffer (20 mM Tris pH 7.4, 1 M NaCl, 10% Glycerol, 10 mM Imidazole, 5 mM KCl, 10
539 mM MgCl2, 2 mM ATP) and low salt buffer (20 mM Tris pH 7.4, 1 M NaCl, 10% Glycerol, 10 mM
540 Imidazole) respectively. The proteins were eluted in elution buffer (20 mM Tris pH 7.4, 150 mM NaCl,
541 10% Glycerol, 250 mM Imidazole) and dialyzed into storage buffer (20 mM Tris pH 7.4, 150 mM NaCl).
542 The contaminant proteins were removed by passing through S200 size exclusion column. The
543 concentrated proteins were stored in -80° C freezer.

544 RNase E CTD purification: His6-MBP-TEV-RNase E CTD was expressed and purified in the same way as
545 described above except the lysis buffer additionally contained 1M NaCl and 0.1% Triton X-100.

546 Hfq purification: Hfq protein was expressed at 18° C for 16 hours. Lysis buffer and elution buffer
547 contained 1 M NaCl instead of 150 mM and 500 mM NaCl respectively. To remove the contaminating
548 nucleic acids, the His tag affinity purified protein was treated with 30 µg/mL RNase A and 5 U/mL DNase
549 I for 1 hour at 37° C, concentrated and loaded onto HiLoad 16/60 Superdex 200 size exclusion column
550 (GE healthcare). The absence of RNase A was further validated by incubating RNA with the protein.

551 **Protein labeling:**

552 Cyanine 5 NHS ester labeling of proteins:

553 Labeling reactions were carried out according to manufacturer's protocol (Lumiprobe). Cy5 NHS ester
554 dye dissolved in DMSO was incubated with proteins at an equal ratio in 0.1M sodium bicarbonate buffer
555 pH 8.5 at room temperature for 4 hours. Protein labeling calculator
556 https://www.lumiprobe.com/calc/protein-labeling was used to calculate the amount of protein and
557 dye used in the labeling reactions. The excess of dye was removed by dialyzing against protein storage
558 buffer (20mM Tris pH 7.4, 150mM NaCl) using a 3 kDa cut off dialysis cassette. Degree of labeling was
559 calculated using the formula:

560 $$number\ of\ cy5\ dye\ per\ protein = \frac{molarity\ of\ cy5\ dye}{molarity\ of\ protein}$$

561 $$[molarity\ of\ cy5\ dye] = \frac{A650}{\varepsilon 650}$$

562 $$molarity\ of\ protein = \frac{A280c}{\varepsilon 280}$$

563 $$A650 = conjugate\ absorbance\ at\ 650nm$$

564 $$\varepsilon 650 = molar\ extinction\ coefficient\ of\ Cy5\ dye$$

565 $$A280c = conjugate\ corrected\ absorbance\ at\ 280nm = A280 - \big(A650 * (0.05)\big)$$

566 $$\varepsilon 280 = molar\ extinction\ coefficient\ of\ protein$$

567 ***In vitro* phase separation experiments and droplet assays**

568 Proteins at their *in vivo* concentrations are incubated in the presence or absence of *C. crescentus* total
569 RNA (20 ng/µL) in 20mM Tris pH 7.4, 100mM NaCl for 30 minutes at room temperature. The mixture
570 was pipetted onto glass slide, covered with a cover slip, and imaged using Nikon epifluorescence

571 microscope. For quantification of number and distribution of droplets, 10 images for each protein were
572 analyzed using 'analyze particles' function in Image J. See table 1 for detailed protocol.

573 For recruitment assays, 6 µM RNAse E CTD was incubated with 20 ng/ µL of *C. crescentus* total RNA in
574 20mM Tris pH 7.4, 100mM NaCl for 20 minutes at room temperature, followed by the addition of Cy5
575 labeled client proteins and additional incubation for 20 minutes before imaging. The level of recruitment
576 was assessed by calculating the partition coefficient of client proteins. 30 droplets were analyzed in each
577 case.

578 $$partition\ coefficient = \frac{mean\ fluorescence\ intensity\ inside\ the\ droplets}{mean\ fluorescence\ intensity\ outside\ the\ droplets}$$

579 ImageJ software was used to quantify the mean fluorescence and the data was plotted in PlotsOfData[64].
580 Coassembly experiments were performed by mixing all the components and incubated for 30 mins at
581 room temperature before imaging.

582 For salt and RNA dependency experiments, preformed protein and RNA condensates were incubated
583 with either varying concentrations of NaCl or RNase A for 30 minutes at room temperature before
584 imaging the solution on a glass slide using phase contrast microscope.

585 RNase E condensation induction in the absence of RNA was carried out by adding client proteins at
586 varied concentrations to 6 µM RNase E CTD in 20mM Tris, 100mM NaCl and incubated for 30 minutes at
587 room temperature. The solution was imaged on a glass slide using phase contrast microscope.

588 ***In-vitro* protein pull down assay**

589 RNAse E CTD tagged with Maltose Binding Protein (MBP) or MBP only was incubated with bait proteins
590 in pull down binding buffer (20mM Hepes pH 7.4, 100mM NaCl, 2% Glycerol, 2mM DTT) for 60 mins at
591 room temperature. 100 µL of Dextrin Agarose resin was added to the above mixture and incubated for
592 another 90 minutes at 4°C on a tube rotator. The samples were washed four times with 1 mL of wash
593 buffer (20mM Hepes pH 7.4, 100mM NaCl) each time. Bound proteins were eluted with 100 µL of
594 elution buffer (20mM Hepes pH 7.4, 150mM NaCl, 10mM Maltose) at 30ºC with constant shaking. The
595 eluted proteins were resolved on SDS PAGE gel.

596 **Electrophoretic mobility shift assay**

597 RNA (50 nM) was incubated with specified concentrations of proteins for 30 mins at room temperature
598 in binding buffer consisting of 20mM Tris pH 7.4, 150mM NaCl, 5% Glycerol, 2mM DTT, 1mM EDTA, 10
599 µg/mL BSA. The incubated samples were resolved on a 5% Acrylamide/Bis-acrylamide native gel
600 (prepared in TBE buffer) at 4ºC in 0.5X TBE running buffer. The gel was stained with SYBR GOLD for
601 20mins and scanned using a Typhoon scanner for RNA/RNA-protein complexes detection.

602 **Determination of order of assembly of RhIE, RNase E and Aconitase foci**

603 *C. crescentus* JS716 (RhIE-YFP/Aconitase-mCherry) and JS452 (RNase E-YFP/Aconitase-mCherry) were
604 grown overnight in PYE medium containing kanamycin (5 µg/mL), spectomycin (25 µg/mL) and
605 streptomycin (5 µg/mL) until the cultures reached mid log-phase (OD~0.3). Prior to imaging, the cells were
606 diluted to 0.05 OD in PYE media and induced with 0.02% xylose for 15 minutes at 28 °C. Aliquots of 1.5 µL
607 of culture were spotted onto pads of 2% agarose in M2G medium and sandwiched between two

608 coverslips. Cells were imaged with an Olympus IX71 inverted epifluorescence microscope with a 100×
609 objective (NA 1.40, oil immersion) kept at 28 °C using at objective heater (Bioptechs). The YFP fusion
610 proteins were imaged under excitation from a 488-nm laser (Coherent Cube 488-50; 0.4 W cm^{-2}) and the
611 mCherry fusions were imaged under excitation from a 561-nm laser (Coherent Sapphire 561-50; 2.0 W
612 cm^{-2}). Both channels were imaged simultaneously on a 512 × 512 pixel Photometric Evolve electron-
613 multiplying charge-coupled device (EMCCD) camera, using an OptoSplit II image splitter (Cairn Research)
614 with a 635-nm long pass filter and a 525/50 nm bandpass filter. An integration time of 250 ms with a delay
615 between frames of 5 s was used, where a shutter blocked irradiation during the delay time to minimize
616 photobleaching of YFP and mCherry.

617 To analyze the fluorescence intensities, the mean intensity of each cell in each channel was first
618 subtracted from the movies. Foci were then detected by eye in the background-subtracted movies, and
619 the mean and maximum intensities within the 9 × 9 pixel region of interest (ROI) surrounding each focus
620 was measured in both channels. Time zero was set to be the frame immediately preceding the first
621 frame with an ROI mean intensity at least 10% higher than the maximum intensity value in the ROI in
622 the previous frame. This time zero was also assigned as time zero on the other channel. Subsequently,
623 the maximum intensity within the ROIs were divided by the maximum intensity of the ROI in the time
624 zero frame to determine the fluorescence intensity enhancement of each focus at each time.

625 **Condensate growth kinetic assays**

626 Time lapse images were acquired using Zeiss LSM 800 microscope. 6 µM of RNase E CTD YFP (RCY) was
627 spotted onto a glass slide, and either the RNA or proteins or both at specified concentrations was
628 pipetted onto RCY solution. The image acquisition was started before the addition of RNA or proteins or
629 both, but the zero-minute time point was calculated from the time they are added to RCY solution on
630 glass slide. The zero-minute time point for 'RCY only' started from the time the sample was spotted onto
631 glass slide. The images were acquired for 2.5 minutes with 50 ms time interval. The data was quantified
632 in Image J and plotted in MS Excel.

633 **FRAP assays**

634 FRAP was performed according to a standard protocol (Jing et al., 2018). Briefly, the measured F(t) over
635 the bleached circular area of d = 2 µm in diameter, normalized by that of the unbleached region of the
636 same diameter, F(0), was fitted by a one-phase exponential function using the "Bottom to (SpaZeisn +
637 Bottom)" analysis as $F(t)/F(0) = Bottom + Span*(1 - \exp(-t \ln 2/\tau_{1/2}))$, where $\tau_{1/2}$ is the halftime for
638 diffusion. The apparent diffusion coefficient, D, of f-dextran in PSBMA–{W12} coacervates was obtained
639 from $\tau_{1/2}$ according to $D = d2/(4\tau_{1/2})$.

640 Figure Legends

641 **Figure 1.** BR-body enrichment proteomics identifies BR-body associated proteins. A) *Caulobacter*
642 *crescentus* BR-body enrichment[30] was performed, followed by LC-MS/MS proteomics to identify BR-body
643 associated proteins. JS299 (an RNase E active site mutant) was used to isolate BR-bodies, and JS221 (an
644 RNase E mutant lacking the C-terminal disordered region that cannot form BR-bodies) was used as a
645 negative control. B) BR-body enrichment analysis from the LC-MS/MS proteomics data. The RNA
646 degradosome proteins were identified by pulldown from[31,34,40]. Polar proteins were identified as
647 interactors with PopZ[65] or polar condensates with interactions with PopZ, PodJ, or SpmX. Polar proteins

648 measured in the negative control but undetected in the BR-body enriched samples were plotted at <-5.
649 T-tests with uneven variance were used for statistical comparison. GO-term enrichment for localization
650 and protein function were performed using NCBI DAVID[66]. C) Localization pattern of foci-forming YFP
651 fusions. All genes were placed under control of the vanillate promoter grown in M2G minimal media. *In*
652 *vivo* protein fusion strains were analyzed at mid-exponential phase of growth (OD 0.3-0.6) following 6-
653 hours of induction with 0.5mM vanillate and quantified using Microbe J[63]. Three replicates were
654 performed in three different days and 3 images were analyzed from each day to calculate the average
655 number of foci/cell. A minimum of 150 cells were used for the analysis. Error bars represent standard
656 error. Raw images in supplementary figure 1(Fig S1).

657 **Figure 2.** RNase E is required for foci localization of most BR-body associated proteins. A) Subcellular
658 localization patterns of *C. crescentus* protein-YFP strains expressed from the *vanA* locus in the RNase E
659 depletion background where the sole copy of the RNase E gene is controlled by the xylose promoter.
660 The YFP intensity of aconitase-YFP was too low to measure when expressed from the vanillate promoter,
661 so a native gene fusion was used instead. YFP intensity of each image was normalized from its brightest
662 level relative to its background level. Depletion strains were analyzed at mid-exponential phase of
663 growth (OD 0.3-0.6) and after 24 hours of depletion of xylose. B) Quantitation of the number of *Ccr*
664 protein-YFP foci per cell measured in M2G minimal media with xylose (+Xyl) and M2G minimal media
665 lacking xylose (-Xyl) for the same strains in panel A. All images were quantified using Microbe-J[63]. Three
666 replicates were performed in three different days and 3 images were analyzed from each day to
667 calculate the average # foci/cell. A minimum of 175 cells were used for the analysis. Error bars represent
668 standard error. Observed dependence on RNase E is indicated on the right.

669 **Figure 3**. Some BR-body enriched proteins can drive RNA dependent biomolecular condensation. A)
670 (Left) Domain organization of proteins that undergo LLPS. The red line indicates disordered region as
671 predicted by PONDR. (Right) Disorderness[67], Pscore[62], Catgranule[68] and DeePhase[69] scores to predict the
672 propensity of LLPS B) Phase contrast microscopy images of the purified proteins incubated at their *in*
673 *vivo* concentrations in standard buffer (20mM Tris pH 7.4, 100mM NaCl, 1mM DTT) in the presence and
674 absence of *C. crescentus* total RNA (30ng/uL). Scale bar is 5 µm. C) Droplets are dissolved by NaCl and
675 RNase A. The dissolution of droplets was tested at different NaCl concentrations (0.1, 0.5 and 1M) and
676 RNase A (1 µg). All the proteins were found to be NaCl and RNase sensitive.

677 **Figure 4.** Many BR-body associated proteins are directly recruited to RNase E condensates *in vitro.* A)
678 Cartoon showing the *in vitro* RNase E droplet recruitment assay. Cy5 labeled proteins are added to
679 preformed RNase E CTD+RNA droplets. Microscopy images of the droplets are taken in Phase contrast
680 and Cy5 fluorescence, and the partition coefficients of the fluorescence signal is calculated for each
681 droplet. B) Partition coefficient (PC) of Cy5 labeled client proteins in RNase E CTD droplets. Negative
682 controls BSA Cy5 and SpmX Cy5 have partition coefficients of 1. The black horizontal line through the
683 plot indicates a PC of 1 which indicates the no enrichment baseline. PC of ribosomal protein S1 and
684 MetK proteins could not be determined because of the dissolution of droplets. The data was quantified
685 in imageJ software and plotted in PlotsofData[64]. For the example images presented, left image is phase
686 contrast and the right image is Cy5 channel of each indicated protein. Scale is 10 µm for all images.

687 **Figure 5.** Ribosomal protein S1 and MetK dissolve BR-bodies *in vitro* and *in vivo.* A) Microscopy images of
688 *in vitro* RNase E droplets incubated with either ribosomal protein S1 or MetK. RNA induced RNase E
689 droplets are shown on the top, while PNPase induced RNase E droplets are shown below. Scale is 10 µm

690 for all images. Below is a proposed cartoon of the RNA dependence of dissolution of each protein. B)
691 RNA and protein binding data for ribosomal protein S1 and MetK with 1 µM RNA. RNA was visualized by
692 sybr gold staining. C) RNase E coIPs with Acontiase and MetK. Co-IP of mbp-RNase using 1 µM RNase E
693 incubated with 5 µM of the indicated proteins. Eluates were run on SDS-PAGE and stained with simply
694 blue safestain (thermofisher). MBP mock reactions were used as a negative control. D) BR-bodies
695 (marked with aconitase-mCherry) are dissolved upon overexpression of ribosomal protein S1 or MetK
696 from the pBX multicopy plasmid. Quantitation of the average Aconitase-mChy foci/cell was performed
697 using Microbe-J and is plotted on the right (error bars represent standard error). A minimum of 700
698 cells were used for the analysis.

699 **Figure 6.** BR-body associated drivers have distinct condensation and client recruitment profiles. A)
700 Scaffold proteins recruit a distinct subset of client proteins. Each RNA degradosome client labeled with
701 Cy5 was tested for recruitment into each BR-body associated scaffold. Each dot in (A) and (B) plots
702 indicate the partition coefficient in a single droplet. Partition coefficient was calculated from at least 50
703 droplets in each case. The data was quantified in imageJ and plotted in PlotsofData. B) BR-body
704 associated scaffolds drive a complex network of dependencies controlling phase separation. Each
705 protein scaffold was incubated with RNA and allowed to phase separate. Then a small concentration of
706 Cy5 labeled proteins were tested for entry into the condensate by measuring the partition coefficients
707 of the Cy5 channel. C) Order of assembly experiments using GFP-RNase E and RhlE-Cy5 condensates.
708 Condensed simultaneously indicates that both proteins were added together before the addition of RNA
709 to trigger condensation, "condensed separately" indicates that both proteins were incubated with RNA
710 yielding separate condensates that were then mixed together. D) Colocalization of YFP tagged proteins
711 with BR-body marker Aconitase-mCherry. Colored arrows indicate the pattern of localization observed
712 for induvial foci. Correlation plot with the correlation value of each channel for many line traces across
713 Aconitase-mCherry Foci. The correlation of YFP and mCherry signal is calculated for each line trace, and
714 each line trace correlation value is plotted as a single dot on the plot. The median value is represented
715 as a black line. Statistics were based upon 2-tailed T-test with unequal variance. E) *In vivo* order of foci
716 assembly. Time-lapse two-color imaging of RhlE-YFP and Aconitase-mCherry proteins was performed, ,
717 and the evolution of the intensity of each focus after formation is plotted. (i) Intensity evolution in cells
718 in which both Aconitase-mCherry and RhlE-YFP condensates are formed approximately at the same
719 time. The middle line indicates the average value, and the colored region represents the standard
720 deviation between all replicate events. N is the number of events imaged. (ii) Cells in which RhlE-YFP
721 condensates were formed first and the subsequent appearance of Aconitase-mCherry in RhlE-YFP
722 condensates was tracked. (iii) Cells in which Aconitase-mCherry condensates were formed first and the
723 subsequent appearance of RhlE-YFP in Aconitase-mCherry condensates was tracked.

724 **Figure 7.** RNA stimulates rapid BR-body condensation *in vitro*. A) Time lapse imaging of RNase E CTD YFP
725 (RCY) condensate formation. 6 µM RCY assembly was monitored either alone or with different
726 combinations of 100ng/µL RNA, 3 µM PNPase, or all degradosome proteins (3 µM PNPase, 2 µM RhlB, 5
727 µM RNase D1, and 5 µM Aconitase) as indicated on the left. All the images were captured at 20X
728 magnification at the time points indicated above. The scale bar is 20 µm. B) Quantification of
729 condensate growth by calculation of % area occupied in the time lapse experiments from panel A. The
730 data was quantified in imageJ, averaged from three independent replicates, and plotted in MS Excel. C)
731 Apparent FRAM recovery for droplets with the indicated composition. Since no RCY condensates are

732 present at 6 µM, the concentration was increased to 30 µM to induce condensates. The values are
733 averages from at least six different droplets, and error bars represent the standard deviation.

734 **Graphical Abstract.** Summary of BR-body protein interactome. Scaffolds/Drivers of phase separation
735 are drawn as blue circles, Protein inhibitors of phase separation are drawn in red circles, and clients of
736 BR-bodies are drawn in green circles. Lines between two protein circles represent a direct interaction.

737 Authors Contribution:

738 VN performed protein purifications, all *in vitro* experiments, and *in vivo* experiments. IWR performed
739 protein purifications, *in vivo* experiments (*in vivo* expression experiments, *in vivo* depletion experiments,
740 and colocalization experiments), and made plasmids and strains for *in vivo* experiments. VN, AH, JV
741 performed droplet kinetic assays and FRAP experiments. KM, AG, and YH purified proteins. NM purified
742 BR bodies for BR-body proteomics. CBM and MC performed LC-MS data collection and analysis. LAOR
743 performed RhlE *in vivo* assemble experiments.

744 Acknowledgements:

745 NIH grant R35GM124733 to JS. NIH grants R01GM143182 and R01GM144731 to JB. NIH Grant
746 R01GM136863 to WSC. NSF grant CMMI-1914436 to YZ. NIH grant R01GM139277 to MC. We would like
747 to acknowledge the Mass Spectrometry and Proteomics Facility at Notre Dame.

748 References:

749 1. Azaldegui, C.A., Vecchiarelli, A.G., and Biteen, J.S. (2021). The emergence of phase separation as
750 an organizing principle in bacteria. Biophysical Journal *120*, 1123–1138. 10.1016/j.bpj.2020.09.023.

751 2. Banani, S.F., Lee, H.O., Hyman, A.A., and Rosen, M.K. (2017). Biomolecular condensates:
752 organizers of cellular biochemistry. Nature Reviews Molecular Cell Biology *18*, 285–298.
753 10.1038/nrm.2017.7.

754 3. Nandana, V., and Schrader, J.M. (2021). Roles of liquid–liquid phase separation in bacterial RNA
755 metabolism. Current Opinion in Microbiology *61*, 91–98. 10.1016/j.mib.2021.03.005.

756 4. Al-Husini, N., Tomares, D.T., Bitar, O., Childers, W.S., and Schrader, J.M. (2018). α-
757 Proteobacterial RNA Degradosomes Assemble Liquid-Liquid Phase-Separated RNP Bodies. Molecular Cell
758 *71*, 1027-1039.e14. 10.1016/j.molcel.2018.08.003.

759 5. Ladouceur, A.-M., Parmar, B.S., Biedzinski, S., Wall, J., Tope, S.G., Cohn, D., Kim, A., Soubry, N.,
760 Reyes-Lamothe, R., and Weber, S.C. (2020). Clusters of bacterial RNA polymerase are biomolecular
761 condensates that assemble through liquid–liquid phase separation. PNAS *117*, 18540–18549.
762 10.1073/pnas.2005019117.

763 6. Lasker, K., von Diezmann, L., Zhou, X., Ahrens, D.G., Mann, T.H., Moerner, W.E., and Shapiro, L.
764 (2020). Selective sequestration of signalling proteins in a membraneless organelle reinforces the spatial
765 regulation of asymmetry in Caulobacter crescentus. Nature Microbiology *5*, 418–429. 10.1038/s41564-
766 019-0647-7.

767 7. McQuail, J., Switzer, A., Burchell, L., and Wigneshweraraj, S. (2020). The RNA-binding protein
768 Hfq assembles into foci-like structures in nitrogen starved Escherichia coli. Journal of Biological
769 Chemistry *295*, 12355–12367. 10.1074/jbc.RA120.014107.

770 8. Monterroso, B., Zorrilla, S., Sobrinos-Sanguino, M., Robles-Ramos, M.A., López-Álvarez, M.,
771 Margolin, W., Keating, C.D., and Rivas, G. (2019). Bacterial FtsZ protein forms phase-separated
772 condensates with its nucleoid-associated inhibitor SlmA. EMBO reports *20*, e45946.
773 10.15252/embr.201845946.

774 9. Wang, H., Yan, X., Aigner, H., Bracher, A., Nguyen, N.D., Hee, W.Y., Long, B.M., Price, G.D., Hartl,
775 F.U., and Hayer-Hartl, M. (2019). Rubisco condensate formation by CcmM in β-carboxysome biogenesis.
776 Nature *566*, 131–135. 10.1038/s41586-019-0880-5.

777 10. Goldberger, O., Szoke, T., Nussbaum-Shochat, A., and Amster-Choder, O. (2022). Heterotypic phase
778 separation of Hfq is linked to its roles as an RNA chaperone. Cell Reports *41*, 111881.
779 10.1016/j.celrep.2022.111881.

780 11. Feng, Z., Chen, X., Wu, X., and Zhang, M. (2019). Formation of biological condensates via phase
781 separation: Characteristics, analytical methods, and physiological implications. Journal of Biological
782 Chemistry *294*, 14823–14835. 10.1074/jbc.REV119.007895.

783 12. Mittag, T., and Pappu, R.V. (2022). A conceptual framework for understanding phase separation
784 and addressing open questions and challenges. Molecular Cell *82*, 2201–2214.
785 10.1016/j.molcel.2022.05.018.

786 13. Kar, M., Dar, F., Welsh, T.J., Vogel, L.T., Kühnemuth, R., Majumdar, A., Krainer, G., Franzmann,
787 T.M., Alberti, S., Seidel, C.A.M., et al. (2022). Phase-separating RNA-binding proteins form
788 heterogeneous distributions of clusters in subsaturated solutions. Proceedings of the National Academy
789 of Sciences *119*, e2202222119. 10.1073/pnas.2202222119.

790 14. Ditlev, J.A., Case, L.B., and Rosen, M.K. (2018). Who's In and Who's Out—Compositional Control
791 of Biomolecular Condensates. Journal of Molecular Biology *430*, 4666–4684. 10.1016/j.jmb.2018.08.003.

792 15. Hubatsch, L., Jawerth, L.M., Love, C., Bauermann, J., Tang, T.D., Bo, S., Hyman, A.A., and Weber,
793 C.A. (2021). Quantitative theory for the diffusive dynamics of liquid condensates. eLife *10*, e68620.
794 10.7554/eLife.68620.

795 16. Taylor, N.O., Wei, M.-T., Stone, H.A., and Brangwynne, C.P. (2019). Quantifying Dynamics in
796 Phase-Separated Condensates Using Fluorescence Recovery after Photobleaching. Biophysical Journal
797 *117*, 1285–1300. 10.1016/j.bpj.2019.08.030.

798 17. Collins, M., Tomares, D.T., Schrader, J.M., and Childers, W.S. (2022). RNase E biomolecular
799 condensates stimulate PNPase activity. 2022.06.06.495039. 10.1101/2022.06.06.495039.

800 18. Peeples, W., and Rosen, M.K. (2021). Mechanistic dissection of increased enzymatic rate in a
801 phase-separated compartment. Nat Chem Biol *17*, 693–702. 10.1038/s41589-021-00801-x.

802 19. Tibble, R.W., Depaix, A., Kowalska, J., Jemielity, J., and Gross, J.D. (2021). Biomolecular
803 condensates amplify mRNA decapping by biasing enzyme conformation. Nat Chem Biol *17*, 615–623.
804 10.1038/s41589-021-00774-x.

805 20. Moon, S.L., Morisaki, T., Khong, A., Lyon, K., Parker, R., and Stasevich, T.J. (2019). Multicolour
806 single-molecule tracking of mRNA interactions with RNP granules. Nat Cell Biol *21*, 162–168.
807 10.1038/s41556-018-0263-4.

808 21. Pitchiaya, S., Mourao, M.D.A., Jalihal, A.P., Xiao, L., Jiang, X., Chinnaiyan, A.M., Schnell, S., and
809 Walter, N.G. (2019). Dynamic Recruitment of Single RNAs to Processing Bodies Depends on RNA
810 Functionality. Molecular Cell *74*, 521-533.e6. 10.1016/j.molcel.2019.03.001.

811 22. Hubstenberger, A., Courel, M., Bénard, M., Souquere, S., Ernoult-Lange, M., Chouaib, R., Yi, Z.,
812 Morlot, J.-B., Munier, A., Fradet, M., et al. (2017). P-Body Purification Reveals the Condensation of
813 Repressed mRNA Regulons. Molecular Cell *68*, 144-157.e5. 10.1016/j.molcel.2017.09.003.

814 23. Jain, S., Wheeler, J.R., Walters, R.W., Agrawal, A., Barsic, A., and Parker, R. (2016). ATPase-
815 Modulated Stress Granules Contain a Diverse Proteome and Substructure. Cell *164*, 487–498.
816 10.1016/j.cell.2015.12.038.

817 24. Khong, A., Matheny, T., Jain, S., Mitchell, S.F., Wheeler, J.R., and Parker, R. (2017). The Stress
818 Granule Transcriptome Reveals Principles of mRNA Accumulation in Stress Granules. Molecular Cell *68*,
819 808-820.e5. 10.1016/j.molcel.2017.10.015.

820 25. Markmiller, S., Soltanieh, S., Server, K.L., Mak, R., Jin, W., Fang, M.Y., Luo, E.-C., Krach, F., Yang,
821 D., Sen, A., et al. (2018). Context-Dependent and Disease-Specific Diversity in Protein Interactions within
822 Stress Granules. Cell *172*, 590-604.e13. 10.1016/j.cell.2017.12.032.

823 26. Youn, J.-Y., Dunham, W.H., Hong, S.J., Knight, J.D.R., Bashkurov, M., Chen, G.I., Bagci, H., Rathod,
824 B., MacLeod, G., Eng, S.W.M., et al. (2018). High-Density Proximity Mapping Reveals the Subcellular
825 Organization of mRNA-Associated Granules and Bodies. Molecular Cell *69*, 517-532.e11.
826 10.1016/j.molcel.2017.12.020.

827 27. Xing, W., Muhlrad, D., Parker, R., and Rosen, M.K. (2020). A quantitative inventory of yeast P
828 body proteins reveals principles of composition and specificity. eLife *9*, e56525. 10.7554/eLife.56525.

829 28. Currie, S.L., Xing, W., Muhlrad, D., Decker, C.J., Parker, R., and Rosen, M.K. (2022). Quantitative
830 reconstitution of yeast RNA processing bodies. 2022.08.13.503854. 10.1101/2022.08.13.503854.

831 29. Al-Husini, N., Tomares, D.T., Pfaffenberger, Z.J., Muthunayake, N.S., Samad, M.A., Zuo, T., Bitar,
832 O., Aretakis, J.R., Bharmal, M.-H.M., Gega, A., et al. (2020). BR-Bodies Provide Selectively Permeable
833 Condensates that Stimulate mRNA Decay and Prevent Release of Decay Intermediates. Molecular Cell
834 *78*, 670-682.e8. 10.1016/j.molcel.2020.04.001.

835 30. Muthunayake, N.S., Al-Husini, N., and Schrader, J.M. (2020). Differential Centrifugation to Enrich
836 Bacterial Ribonucleoprotein Bodies (BR bodies) from Caulobacter crescentus. STAR Protocols *1*, 100205.
837 10.1016/j.xpro.2020.100205.

838 31. Hardwick, S.W., Chan, V.S.Y., Broadhurst, R.W., and Luisi, B.F. (2011). An RNA degradosome
839 assembly in Caulobacter crescentus. Nucleic Acids Res *39*, 1449–1459. 10.1093/nar/gkq928.

840 32. Canestrari, J.G., Lasek-Nesselquist, E., Upadhyay, A., Rofaeil, M., Champion, M.M., Wade, J.T.,
841 Derbyshire, K.M., and Gray, T.A. (2020). Polycysteine-encoding leaderless short ORFs function as

842 cysteine-responsive attenuators of operonic gene expression in mycobacteria. Molecular Microbiology
843 *114*, 93–108. 10.1111/mmi.14498.

844 33. Mousseau, C.B., Pierre, C.A., Hu, D.D., and Champion, M.M. (2022). Miniprep assisted
845 proteomics (MAP) for rapid proteomics sample preparation. Anal. Methods, 10.1039.D2AY01549H.
846 10.1039/D2AY01549H.

847 34. Voss, J.E., Luisi, B.F., and Hardwick, S.W. (2014). Molecular recognition of RhlB and RNase D in
848 the Caulobacter crescentus RNA degradosome. Nucleic Acids Research *42*, 13294–13305.
849 10.1093/nar/gku1134.

850 35. Russell, J.H., and Keiler, K.C. (2009). Subcellular localization of a bacterial regulatory RNA.
851 Proceedings of the National Academy of Sciences *106*, 16405–16409. 10.1073/pnas.0904904106.

852 36. Werner, J.N., Chen, E.Y., Guberman, J.M., Zippilli, A.R., Irgon, J.J., and Gitai, Z. (2009).
853 Quantitative genome-scale analysis of protein localization in an asymmetric bacterium. Proceedings of
854 the National Academy of Sciences *106*, 7858–7863. 10.1073/pnas.0901781106.

855 37. Aretakis, J.R., Gega, A., and Schrader, J.M. (2019). Absolute Measurements of mRNA Translation
856 in Caulobacter crescentus Reveal Important Fitness Costs of Vitamin B12 Scavenging. mSystems *4*,
857 e00170-19. 10.1128/mSystems.00170-19.

858 38. Hondele, M., Sachdev, R., Heinrich, S., Wang, J., Vallotton, P., Fontoura, B.M.A., and Weis, K.
859 (2019). DEAD-box ATPases are global regulators of phase-separated organelles. Nature *573*, 144–148.
860 10.1038/s41586-019-1502-y.

861 39. Beaufay, F., Amemiya, H.M., Guan, J., Basalla, J., Meinen, B.A., Chen, Z., Mitra, R., Bardwell,
862 J.C.A., Biteen, J.S., Vecchiarelli, A.G., et al. (2021). Polyphosphate drives bacterial heterochromatin
863 formation. Science Advances *7*, eabk0233. 10.1126/sciadv.abk0233.

864 40. Aguirre, A.A., Vicente, A.M., Hardwick, S.W., Alvelos, D.M., Mazzon, R.R., Luisi, B.F., and
865 Marques, M.V. (2017). Association of the Cold Shock DEAD-Box RNA Helicase RhlE to the RNA
866 Degradosome in Caulobacter crescentus. Journal of Bacteriology *199*, e00135-17. 10.1128/JB.00135-17.

867 41. Thanbichler, M., Iniesta, A.A., and Shapiro, L. (2007). A comprehensive set of plasmids for
868 vanillate- and xylose-inducible gene expression in Caulobacter crescentus. Nucleic Acids Res. *35*, e137.
869 10.1093/nar/gkm818.

870 42. Tauber, D., Tauber, G., Khong, A., Van Treeck, B., Pelletier, J., and Parker, R. (2020). Modulation
871 of RNA Condensation by the DEAD-Box Protein eIF4A. Cell *180*, 411-426.e16. 10.1016/j.cell.2019.12.031.

872 43. Assis, N.G., Ribeiro, R.A., Silva, L.G. da, Vicente, A.M., Hug, I., and Marques, M.V. (2019).
873 Identification of Hfq-binding RNAs in Caulobacter crescentus. RNA Biology *16*, 719–726.
874 10.1080/15476286.2019.1593091.

875 44. Møller, T., Franch, T., Højrup, P., Keene, D.R., Bächinger, H.P., Brennan, R.G., and Valentin-
876 Hansen, P. (2002). Hfq: A Bacterial Sm-like Protein that Mediates RNA-RNA Interaction. Molecular Cell *9*,
877 23–30. 10.1016/S1097-2765(01)00436-1.

878 45. Updegrove, T.B., Zhang, A., and Storz, G. (2016). Hfq: the flexible RNA matchmaker. Curr Opin
879 Microbiol *30*, 133–138. 10.1016/j.mib.2016.02.003.

880 46. Urban, J.H., and Vogel, J. (2008). Two Seemingly Homologous Noncoding RNAs Act Hierarchically
881 to Activate glmS mRNA Translation. PLOS Biology *6*, e64. 10.1371/journal.pbio.0060064.

882 47. Vogel, J., and Luisi, B.F. (2011). Hfq and its constellation of RNA. Nat Rev Microbiol *9*, 578–589.
883 10.1038/nrmicro2615.

884 48. Ikeda, Y., Yagi, M., Morita, T., and Aiba, H. (2011). Hfq binding at RhlB-recognition region of
885 RNase E is crucial for the rapid degradation of target mRNAs mediated by sRNAs in Escherichia coli.
886 Molecular Microbiology *79*, 419–432. 10.1111/j.1365-2958.2010.07454.x.

887 49. Fei, J., Singh, D., Zhang, Q., Park, S., Balasubramanian, D., Golding, I., Vanderpool, C.K., and Ha,
888 T. (2015). Determination of in vivo target search kinetics of regulatory noncoding RNA. Science *347*,
889 1371–1374. 10.1126/science.1258849.

890 50. Duval, M., Korepanov, A., Fuchsbauer, O., Fechter, P., Haller, A., Fabbretti, A., Choulier, L.,
891 Micura, R., Klaholz, B.P., Romby, P., et al. (2013). Escherichia coli Ribosomal Protein S1 Unfolds
892 Structured mRNAs Onto the Ribosome for Active Translation Initiation. PLOS Biology *11*, e1001731.
893 10.1371/journal.pbio.1001731.

894 51. Delvillani, F., Papiani, G., Dehò, G., and Briani, F. (2011). S1 ribosomal protein and the interplay
895 between translation and mRNA decay. Nucleic Acids Res *39*, 7702–7715. 10.1093/nar/gkr417.

896 52. Robledo, M., García-Tomsig, N.I., Matia-González, A.M., García-Rodríguez, F.M., and Jiménez-
897 Zurdo, J.I. (2021). Synthetase of the methyl donor S-adenosylmethionine from nitrogen-fixing α-rhizobia
898 can bind functionally diverse RNA species. RNA Biology *18*, 1111–1123.
899 10.1080/15476286.2020.1829365.

900 53. Britos, L., Abeliuk, E., Taverner, T., Lipton, M., McAdams, H., and Shapiro, L. (2011). Regulatory
901 Response to Carbon Starvation in Caulobacter crescentus. PLOS ONE *6*, e18179.
902 10.1371/journal.pone.0018179.

903 54. Cabrera, J.E., Cagliero, C., Quan, S., Squires, C.L., and Jin, D.J. (2009). Active Transcription of
904 rRNA Operons Condenses the Nucleoid in Escherichia coli: Examining the Effect of Transcription on
905 Nucleoid Structure in the Absence of Transertion. Journal of Bacteriology *191*, 4180–4185.
906 10.1128/JB.01707-08.

907 55. Queiroz, R.M.L., Smith, T., Villanueva, E., Marti-Solano, M., Monti, M., Pizzinga, M., Mirea, D.-
908 M., Ramakrishna, M., Harvey, R.F., Dezi, V., et al. (2019). Comprehensive identification of RNA–protein
909 interactions in any organism using orthogonal organic phase separation (OOPS). Nat Biotechnol *37*, 169–
910 178. 10.1038/s41587-018-0001-2.

911 56. Shchepachev, V., Bresson, S., Spanos, C., Petfalski, E., Fischer, L., Rappsilber, J., and Tollervey, D.
912 (2019). Defining the RNA interactome by total RNA-associated protein purification. Molecular Systems
913 Biology *15*, e8689. 10.15252/msb.20188689.

914 57. Hentze, M.W., Castello, A., Schwarzl, T., and Preiss, T. (2018). A brave new world of RNA-binding
915 proteins. Nat Rev Mol Cell Biol *19*, 327–341. 10.1038/nrm.2017.130.

916 58. Riback, J.A., Katanski, C.D., Kear-Scott, J.L., Pilipenko, E.V., Rojek, A.E., Sosnick, T.R., and
917 Drummond, D.A. (2017). Stress-Triggered Phase Separation Is an Adaptive, Evolutionarily Tuned
918 Response. Cell *168*, 1028-1040.e19. 10.1016/j.cell.2017.02.027.

919 59. Evinger, M., and Agabian, N. (1977). Envelope-associated nucleoid from Caulobacter crescentus
920 stalked and swarmer cells. Journal of Bacteriology *132*, 294–301. 10.1128/jb.132.1.294-301.1977.

921 60. Schrader, J.M., and Shapiro, L. (2015). Synchronization of Caulobacter Crescentus for
922 Investigation of the Bacterial Cell Cycle. JoVE (Journal of Visualized Experiments), e52633.
923 10.3791/52633.

924 61. Cronin, R.M., Ferrell, M.J., Cahir, C.W., Champion, M.M., and Champion, P.A. (2022). Proteo-
925 genetic analysis reveals clear hierarchy of ESX-1 secretion in Mycobacterium marinum. Proceedings of
926 the National Academy of Sciences *119*, e2123100119. 10.1073/pnas.2123100119.

927 62. Vernon, R.M., Chong, P.A., Tsang, B., Kim, T.H., Bah, A., Farber, P., Lin, H., and Forman-Kay, J.D.
928 (2018). Pi-Pi contacts are an overlooked protein feature relevant to phase separation. eLife *7*, e31486.
929 10.7554/eLife.31486.

930 63. Ducret, A., Quardokus, E.M., and Brun, Y.V. (2016). MicrobeJ, a tool for high throughput
931 bacterial cell detection and quantitative analysis. Nat Microbiol *1*, 1–7. 10.1038/nmicrobiol.2016.77.

932 64. Postma, M., and Goedhart, J. (2019). PlotsOfData—A web app for visualizing data together with
933 their summaries. PLOS Biology *17*, e3000202. 10.1371/journal.pbio.3000202.

934 65. Holmes, J.A., Follett, S.E., Wang, H., Meadows, C.P., Varga, K., and Bowman, G.R. (2016).
935 Caulobacter PopZ forms an intrinsically disordered hub in organizing bacterial cell poles. Proceedings of
936 the National Academy of Sciences *113*, 12490–12495. 10.1073/pnas.1602380113.

937 66. Sherman, B.T., Hao, M., Qiu, J., Jiao, X., Baseler, M.W., Lane, H.C., Imamichi, T., and Chang, W.
938 (2022). DAVID: a web server for functional enrichment analysis and functional annotation of gene lists
939 (2021 update). Nucleic Acids Research *50*, W216–W221. 10.1093/nar/gkac194.

940 67. Romero, P., Obradovic, Z., Kissinger, C., Villafranca, J.E., and Dunker, A.K. (1997). Identifying
941 disordered regions in proteins from amino acid sequence. In Proceedings of International Conference on
942 Neural Networks (ICNN'97), pp. 90–95 vol.1. 10.1109/ICNN.1997.611643.

943 68. Bolognesi, B., Lorenzo Gotor, N., Dhar, R., Cirillo, D., Baldrighi, M., Tartaglia, G.G., and Lehner, B.
944 (2016). A Concentration-Dependent Liquid Phase Separation Can Cause Toxicity upon Increased Protein
945 Expression. Cell Reports *16*, 222–231. 10.1016/j.celrep.2016.05.076.

946 69. Saar, K.L., Morgunov, A.S., Qi, R., Arter, W.E., Krainer, G., Lee, A.A., and Knowles, T.P.J. (2021).
947 Learning the molecular grammar of protein condensates from sequence determinants and embeddings.
948 Proceedings of the National Academy of Sciences *118*, e2019053118. 10.1073/pnas.2019053118.

949

Figure 1

A. BR-body enrichment assay

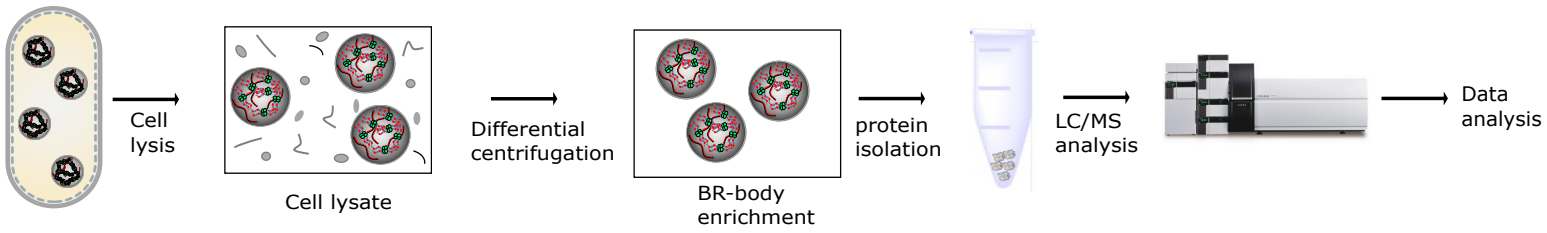

B.

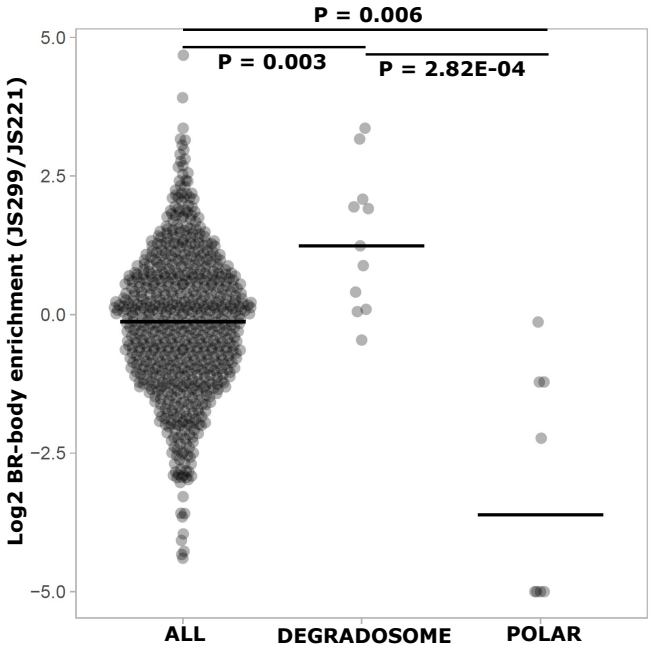

Enriched	Number of proteins	p-value
Cytoplasm	32	9.40E-11
Depleted		
Membrane	160	3.90E-23
Transmembrane	126	2.30E-12
Cell inner membrane	33	3.00E-12
Transmembrane helix	121	3.80E-11
Cell membrane	40	4.30E-11
Cell outer membrane	7	1.30E-03
Cell wall	5	6.40E-02

Enriched	Number of proteins	p-value
RNA Binding	14	9.00E-07
ATP Binding	19	8.80E-03
RNA Degradation	5	9.90E-03
GTPase Activity	5	3.80E-03

C.

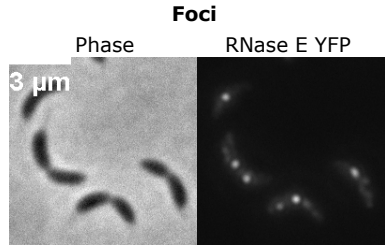

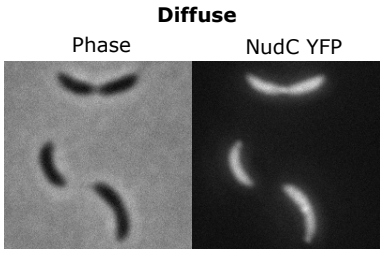

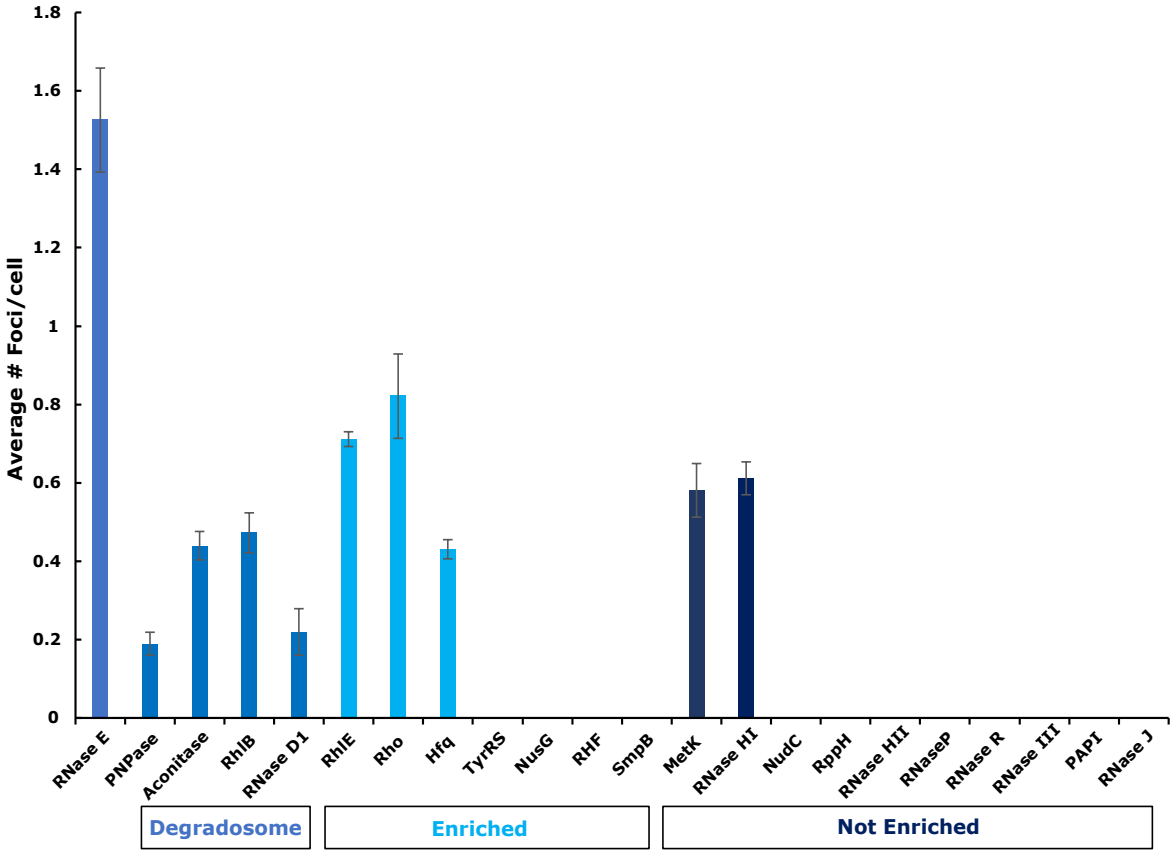

Figure 2

A.

Xylose Dependent RNase E Depletion strain

+Xyl -Xyl

Aconitase YFP

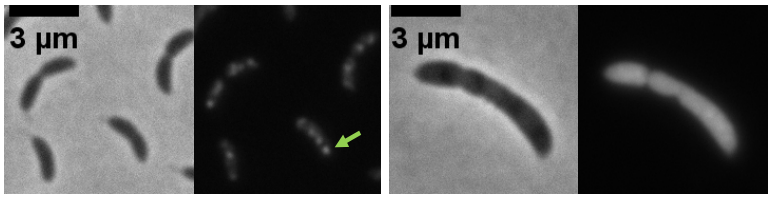

RNase D1 YFP

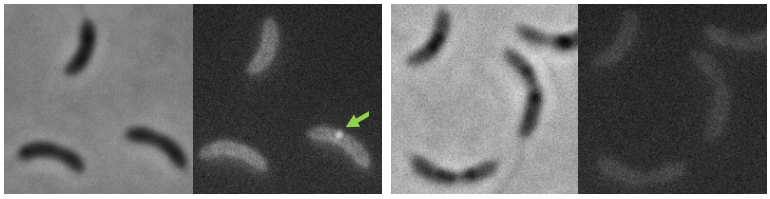

Hfq YFP

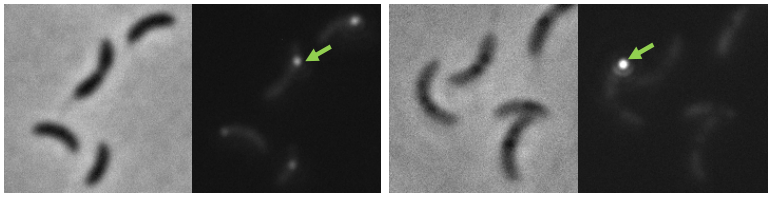

Rho YFP

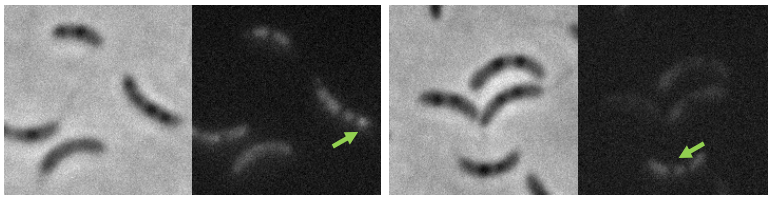

MetK YFP

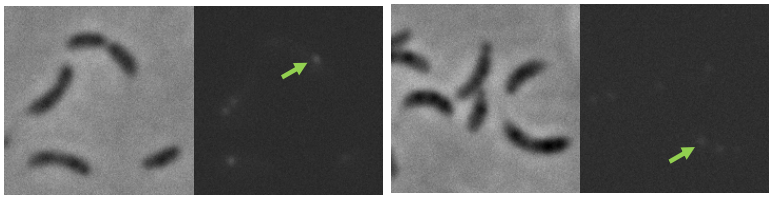

RhlE YFP

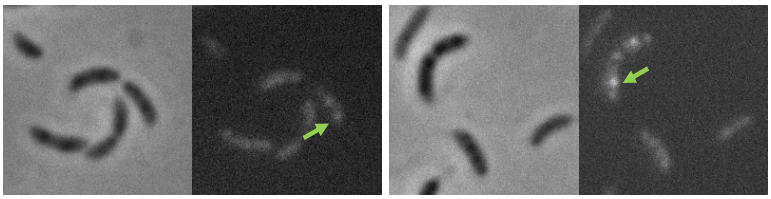

B.

+Xyl -Xyl

RNase E Dependence

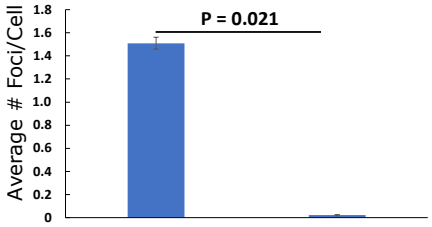

+++

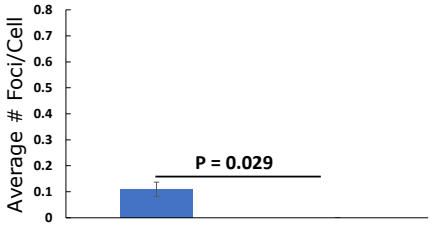

+++

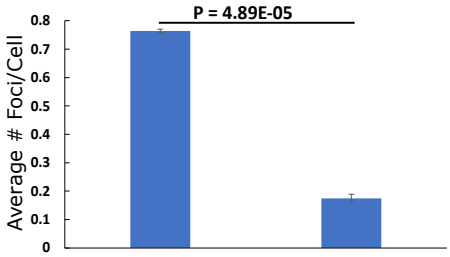

+++

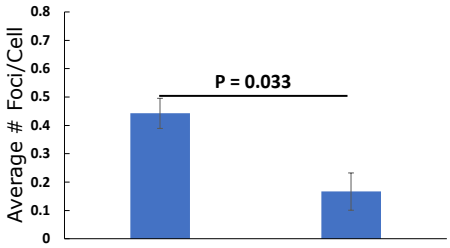

++

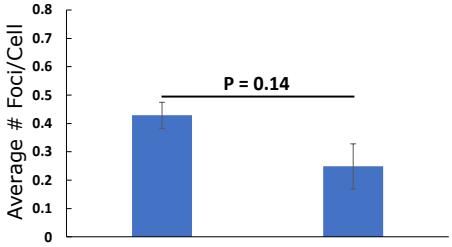

-

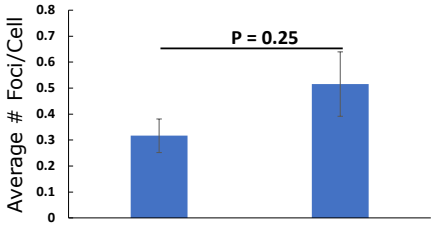

-

Figure 3

A.

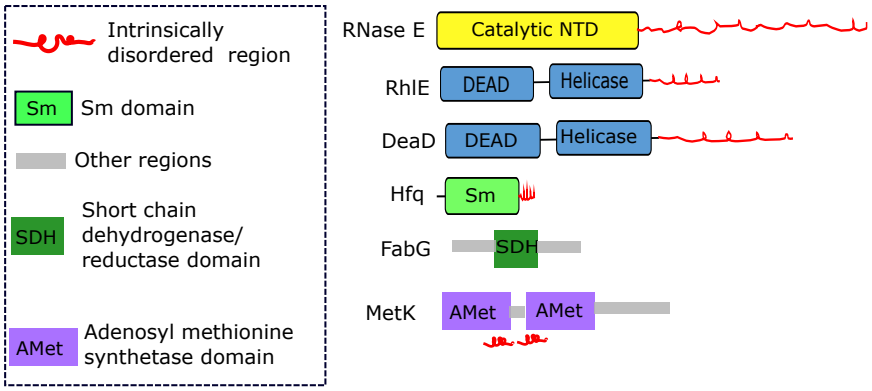

Protein	Disorderness %	Pscore	Catgranule	Deephase
RNase E	35.9	3.72	1.26	0.79
RhlE	17.23	1.29	1.04	0.58
deaD	32.79	4.48	1.04	0.76
Hfq	0	-0.83	-1.06	0.1
FabG	0	-0.02	0.96	0.1
MetK	0	0.15	-0.068	0.22

B.

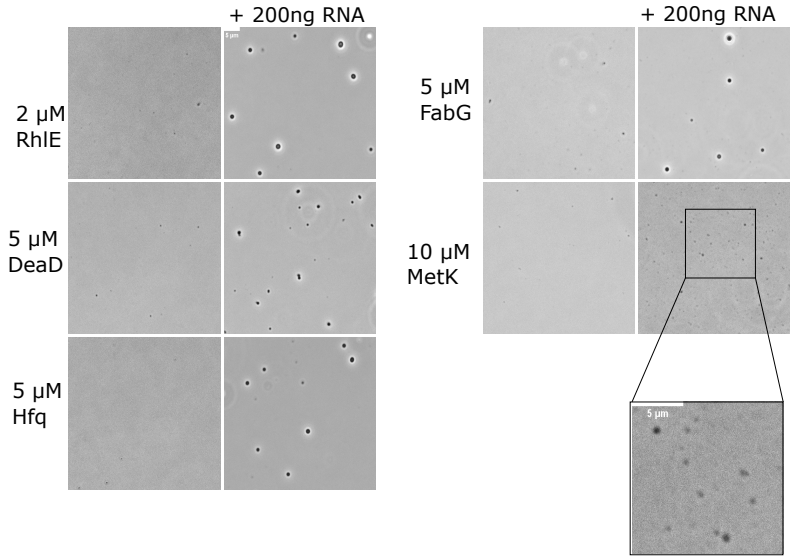

C.

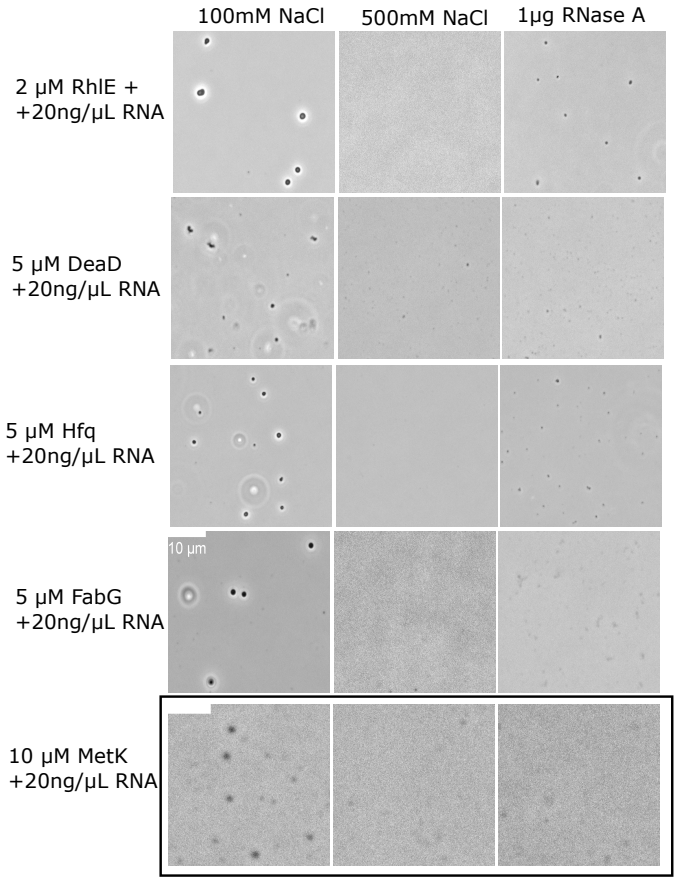

Figure 4

A.

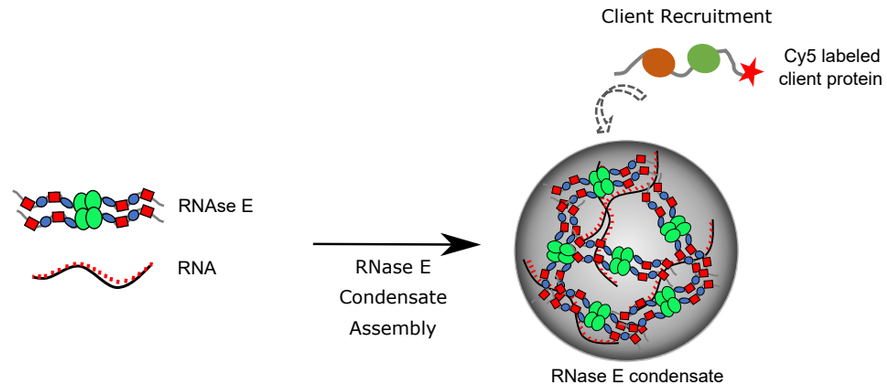
Client Recruitment
Cy5 labeled
client protein
RNAse E
RNA
RNase E
Condensate
Assembly
RNase E condensate

B.

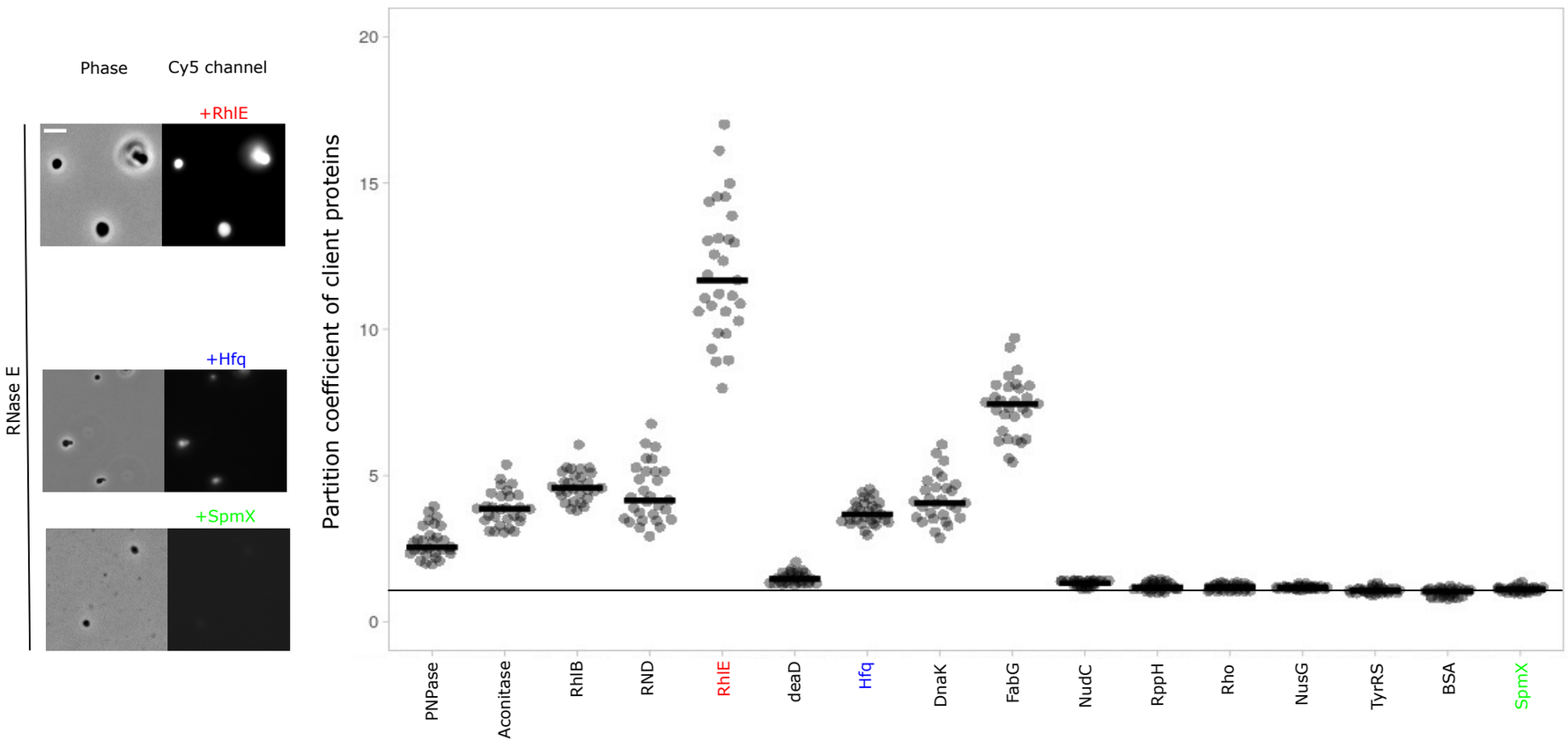
Phase
Cy5 channel
+RhlE
+Hfq
+SpmX
RNase E
Partition coefficient of client proteins
20
15
10
5
0
PNPase
Aconitase
RhlB
RND
RhlE
deaD
Hfq
DnaK
FabG
NudC
RppH
Rho
NusG
TyrRS
BSA
SpmX

Figure 5

A.

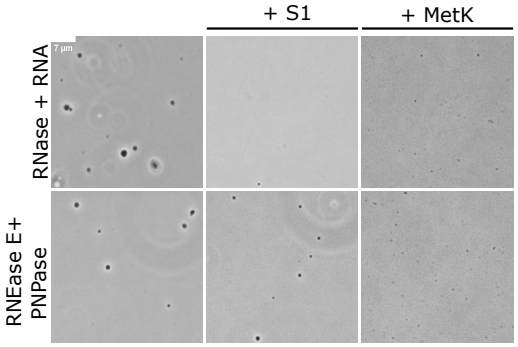

B.

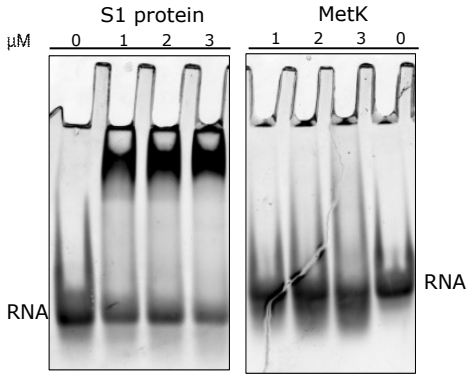

C.

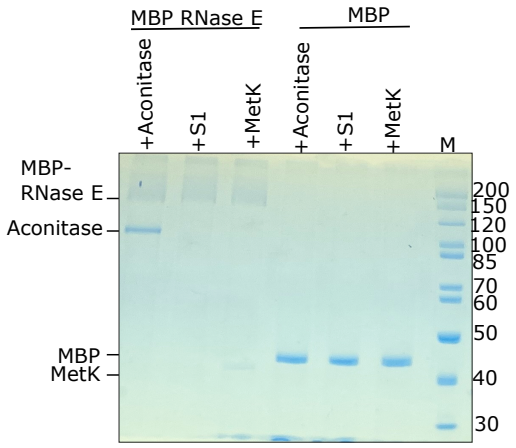

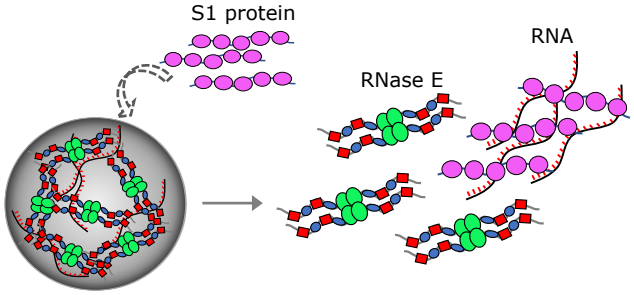

S1 protein dissolution occurs via RNA binding

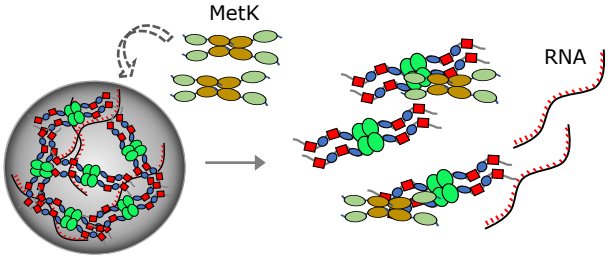

MetK dissolution occurs via RNase E binding

D

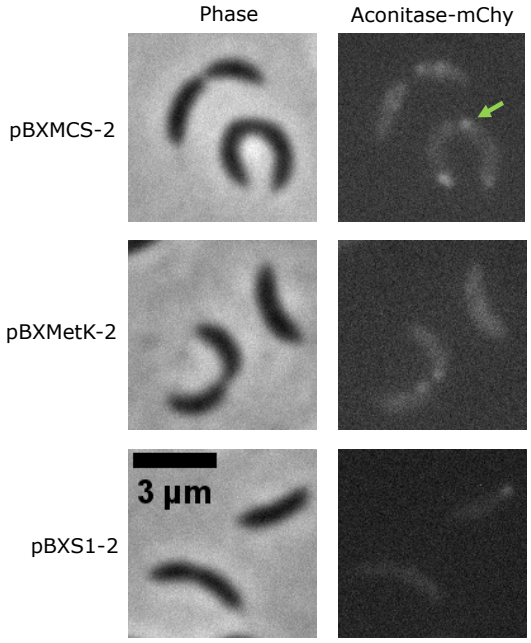

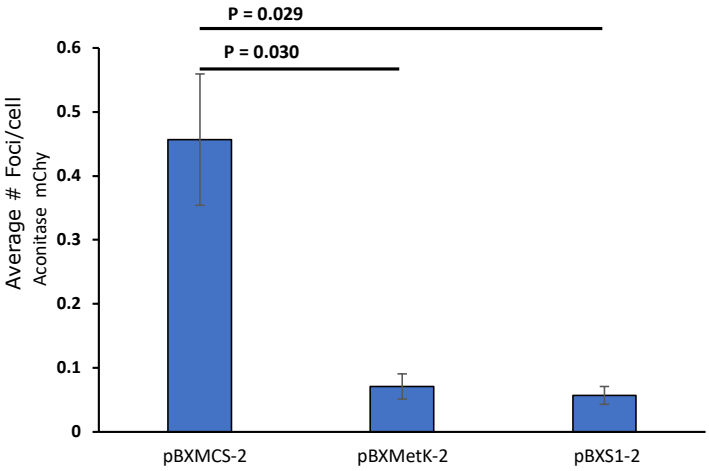

Figure 6

A.

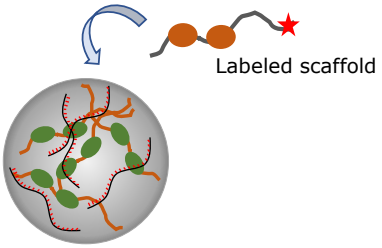

+RNA Scaffold	Labeled Scaffold: RNase E	RhlE	DeaD	Hfq	FabG
RNase E	X	11	1.5	7.5	3.8
RhlE	1.6	X	1.5	2.5	2.5
DeaD	1.7	7.6	X	3.3	2.6
Hfq	ND	4.3	1.8	X	2.4
FabG	1.9	7.4	1.5	3.4	X

Partition Coefficient

15	High
10	
5	
1	Low

B.

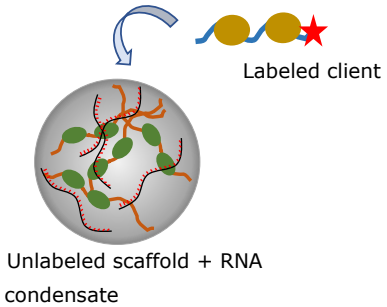

-RNA Scaffold	Labeled client: RhlB	PNP	Aco	RND
RNase E	4.7	2.6	4	4
RhlE	1.0	1.0	1.0	1.0
DeaD	1.5	1.5	1.5	1.5
Hfq	2.3	1.7	2.5	1.7
FabG	1.5	1.7	1.5	1.6

C.

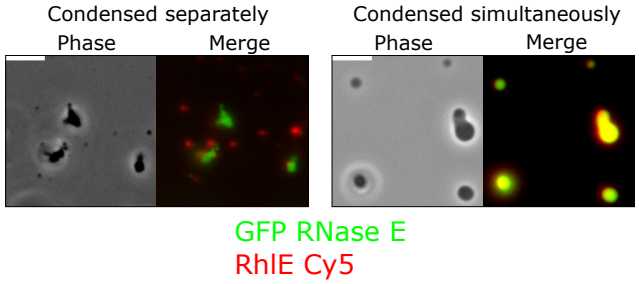

D.

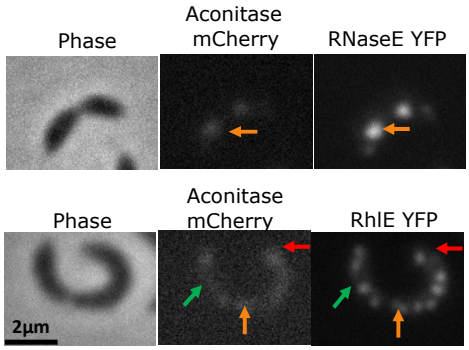

Equal Aconitase/Equal RhlE
High Aconitase/Low RhlE
Low Aconitase/High RhlE

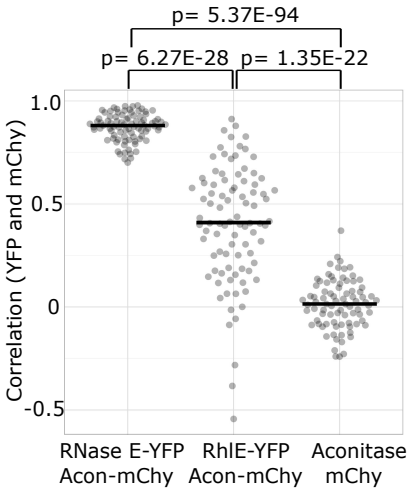

E.

(i)

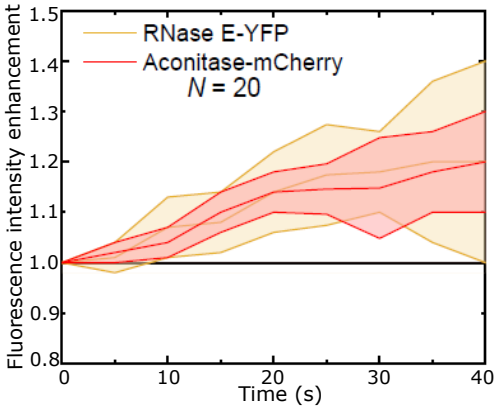

(ii)

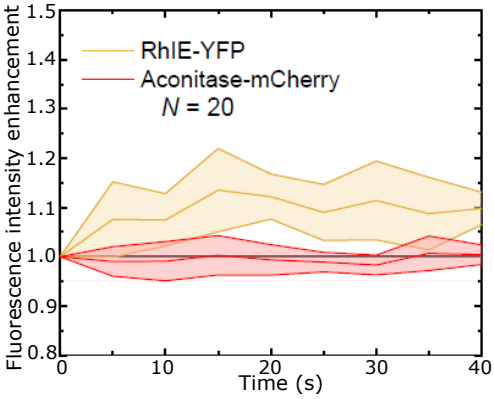

(iii)

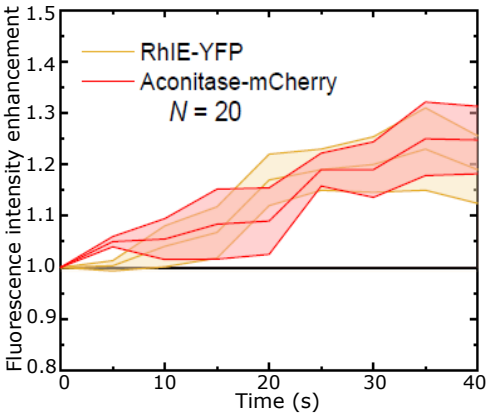

Figure 7

A.

Kinetics of RNase E Condensation

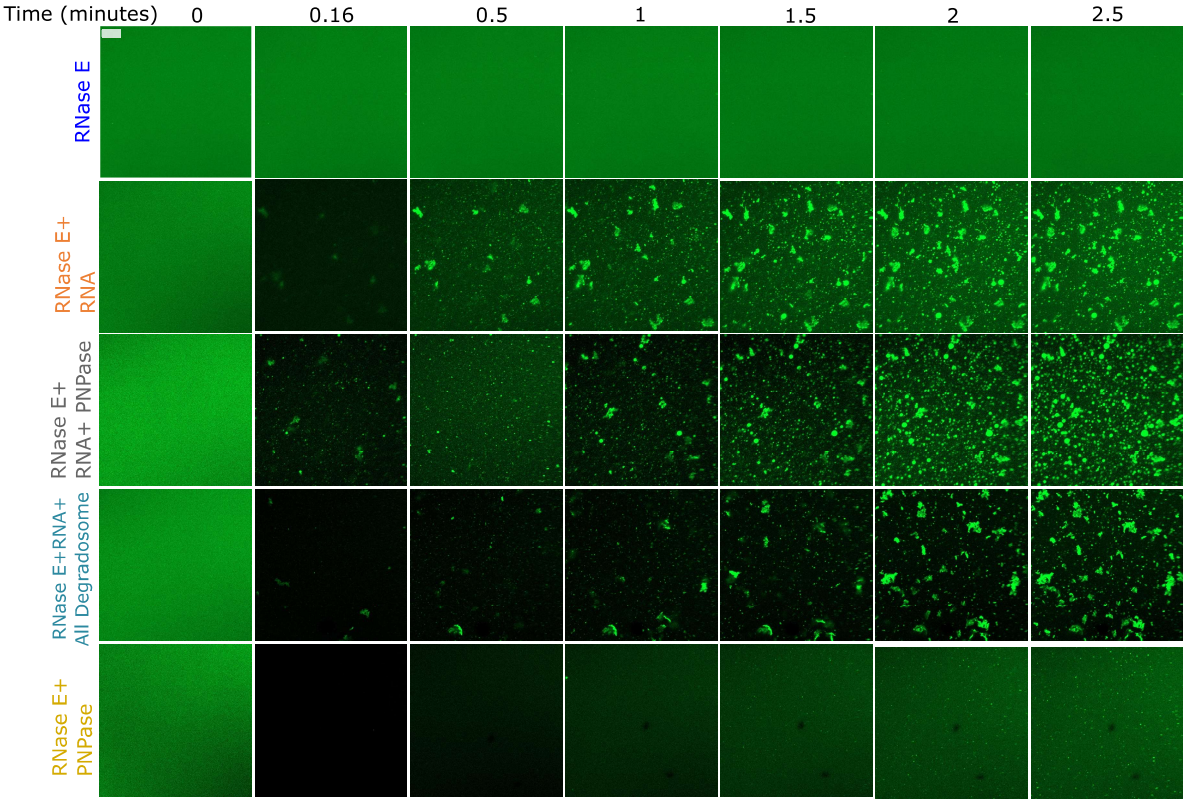

B.

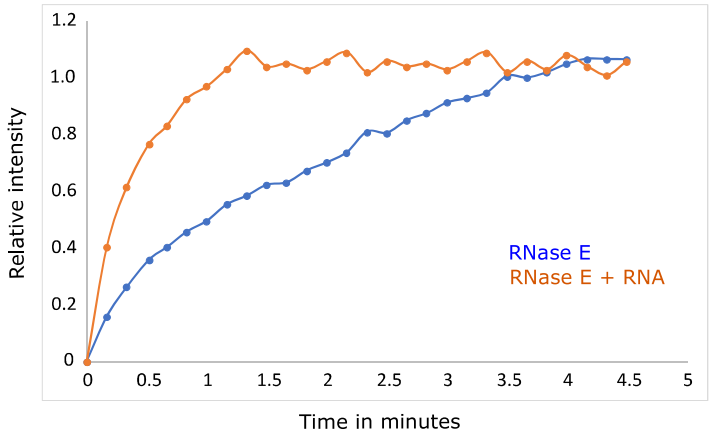
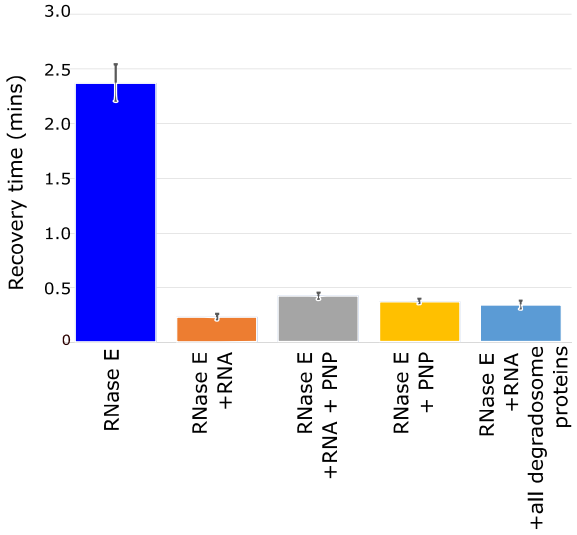
C.